8-2016

Measurement of the Electron Return Effect Using PRESAGE Dosimeter

Gye Won Choi

Recommended Citation

Choi, Gye Won, "Measurement of the Electron Return Effect Using PRESAGE Dosimeter" (2016). *UT GSBS Dissertations and Theses (Open Access)*. Paper 690.

MEASUREMENT OF THE ELECTRON RETURN EFFECT USING PRESAGE® DOSIMETERS

by

Gye Won Choi

APPROVED:

Geoffrey S. Ibbott, Ph.D.
Advisory Professor

David S. Followill, Ph.D.

Laurence E. Court, Ph.D.

Zhifei Wen, Ph.D.

Shouhao Zhou, Ph.D.

APPROVED:

Dean, The University of Texas
Graduate School of Biomedical Sciences at Houston

MEASUREMENT OF THE ELECTRON RETURN EFFECT USING PRESAGE® DOSIMETERS

A

THESIS

Presented to the Faculty of
The University of Texas
Health Science Center at Houston
and
The University of Texas
MD Anderson Cancer Center
Graduate School of Biomedical Sciences
in Partial Fulfillment

of the Requirements

for the Degree of

MASTER OF SCIENCE

by

Gye Won Choi
Houston, Texas

August, 2016

Dedication

To everyone who have seen me and supported me in any way,
during my time in graduate school—

This life would not have been possible without you.

Acknowledgements

First, I would like to thank my advisor Dr. Geoffrey Ibbott for bringing me into the lab when I was at the most confused and weak stage in my life. Through the years I have spent in your lab, you always gave me enough time to remain confused and then to finally figure the solution out myself, through which I overcame my fear for diving into the unknown and for hands-on experiments. I also thank the rest of my committee members—Dr. Laurence Court, Dr. David Followill, Dr. Zhifei Wen, and Dr. Shouhao Zhou—for guiding me through my research.

The lab introduced me to the people that had been essential for me in getting through my research. First and foremost, thank you to my “optical-CT parents,” Ryan Lafratta, Mitchell Carroll, and Slade Klawikowski, for being so patient with me in my learning process, and Mamdooh Alqathami, for making my dosimeters. I would not have been able to get through my graduate research experience without the support from the rest of the lab group—Yvonne Roed and Hannah Lee as well. Special thanks to Ashley Rubinstein, for all you have done to set up the electromagnet and train me in using the magnet. The help from the physicists on Elekta VERSA 1—Jared Ohrt and Ramaswamy Sadagopan—had also been essential.

I would also like to thank the machine shop people: John Costales, Kelly Tharp and Michael Potocsny—without your cooperation, this research would not have been completed as desired. Collaborators from outside MD Anderson (Csaba Pinter, Ting Fung Ma and Chun Yip Yau) have also provided immense support for the implementation and use of their software and codes.

This page does not fully express how grateful I am for all the help and care I have received, because if it were fully expressed, I would be writing another one hundred pages. Above all, thank you to my parents, who have supported me and never gave up on my potential interest in the medical field. And thank you, Jeong Hwan Kook, only god knows how much thanks I owe you for always being there for me as my biggest supporter.

MEASUREMENT OF THE ELECTRON RETURN EFFECT USING PRESAGE® DOSIMETERS

Gye Won Choi

Advisory Professor: Geoffrey Ibbott, Ph.D.

MR-guided radiation therapy (MRgRT) provides benefits such as superior soft tissue contrast, no imaging dose, and functional imaging capacities, but it also has concerns to be addressed. The electron return effect (ERE) refers to dose enhancement at the interface between different media, caused when radiation is delivered in the magnetic field. The ERE poses clinical concerns in MRgRT because it significantly enhances the dose at interfaces, and the intensity and pattern of the dose enhancement depends on many factors. The ERE results in a complex pattern of dose enhancement over a three-dimensional (3D) volume around tissue interfaces inside the patient body, giving rise to the need for 3D dosimetry. If proven reliable in the magnetic field, 3D dosimetry will provide a more rigorous means for the quality assurance (QA) of MRgRT than two-dimensional dosimetry. The 3D dosimeters can also be used to estimate the volumetric dose distribution in MRgRT treatment of heterogeneous treatment sites (e.g., lung), around simple structures such as the trachea and the esophagus, and in MR-guided brachytherapy.

In this thesis, the performance of PRESAGE® in the magnetic field was evaluated by investigating how well PRESAGE® could measure the ERE. The radiation response of Gafchromic® EBT3 film was shown to be unaffected by the magnetic field in a previous study, and the reliability of EBT3 film measurement in the magnetic field was independently verified in this thesis. As a result, the performance of PRESAGE® was evaluated by comparing against EBT3. Before measuring the volumetric ERE, the in-house made PRESAGE® formulation that was used throughout this thesis was tested for magnetic field effects. The formulation showed ~ 9 % under-response when irradiated in the magnetic field, but the response remained strictly linear and thus did not interfere with using

PRESAGE® as a relative dosimeter. Finally, it was hypothesized that the measurement of the ERE using PRESAGE® would agree with EBT3 within 5 %/3 mm local gamma criteria. The EBT3 and PRESAGE® measurements agreed well with a passing rate over 90 %. The hypothesis was proven correct and showed that PRESAGE® is a promising material for the QA of MRgRT.

Table of Contents

Approval page i

Title page........ ii

Dedication........ iii

Acknowledgements iv

Abstract........ v

List of Figures x

List of Tables........ xiii

Chapter 1 - Introduction 1

1.1. Introduction to radiation therapy........ 1

1.2. Development of MRgRT........ 2

1.3. Implication for the quality assurance (QA) of MRgRT equipment........ 5

1.3.1. 2D dosimetry and 3D dosimetry........ 5

1.3.2. PRESAGE® 6

1.4. PRESAGE® dosimetry using Optical-CT system 8

1.4.1. Optical-CT system........ 8

1.4.2. Duke Mid-sized Optical-CT System (DMOS) 10

1.4.3. Edge artifact........ 13

1.5. Dosimeters in magnetic field........ 17

1.6. Gamma analysis 17

1.7. Validity of the PRESAGE®-optical-CT system 20

1.8. General problem area 21

1.9. Hypothesis and Specific Aims 21

Chapter 2 - Specific Aim 1 24

2.1. Rationale 24

2.2. Methods 24

2.2.1. Verifying dose response of in-house made PRESAGE® dosimeters 24

2.2.2. Methods to reduce the edge artifact 25

2.2.3. Determining the region of edge artifact 27

2.3. Results 29

2.3.1. Verifying dose response of in-house made PRESAGE® dosimeters 29

2.3.2. Methods to reduce the edge artifact 31

2.3.3. Determining the region of edge artifact using change-point detection code 35

2.4. Discussion 37

Chapter 3 - Specific Aim 2 39

3.1. Rationale 39

3.2. Methods 39

3.2.1. Setup for irradiations involving magnetic field 39

3.2.2. Magnetic field effects on Gafchromic® EBT3 44

3.2.3. Magnetic field effects on PRESAGE® 45

3.3. Results 46

3.3.1. Calibration of Gafchromic® EBT3 46

3.3.2. Magnetic field effects on EBT3 ... 48

3.3.3. Magnetic field effects on PRESAGE® ... 49

3.4. Discussion ... 51

Chapter 4—Specific Aim 3 ... 53

4.1. Rationale ... 53

4.2. Methods ... 53

4.2.1. Validating workflow: baseline for film-PRESAGE® comparison ... 53

4.2.2. Measurement of the ERE using film and PRESAGE® dosimeters ... 57

4.3. Results ... 60

4.3.1. Validating workflow: baseline for film-PRESAGE® comparison ... 60

4.3.2. Measurement of the ERE using film and PRESAGE® dosimeters ... 61

4.4. Discussion ... 64

4.4.1. Validating workflow: baseline for film-PRESAGE® comparison ... 64

4.4.2. Measurement of the ERE using film and PRESAGE® dosimeters ... 64

Chapter 5 – Conclusion ... 67

Appendix A. Change-point detection method ... 69

Appendix B. Testing for the validity of the gamma analysis on 3D Slicer ... 71

Appendix C. Codes and data ... 73

Bibliography ... 78

VITA ... 83

List of Figures

Figure 1: Sketch of the MR-linac system concept. 3

Figure 2: (Left) Trajectory of a secondary electron and schematic demonstration the ERE. 4

Figure 3: (Left) Monte-Carlo simulation result showing the dose profile along the central beam axis through water-air-water interface and (right) film measurement of the dose profile along the central beam axis through plastic-air-plastic interface [3]. 5

Figure 4: Design of the prototype optical-CT [19]. 9

Figure 5: Schematic of the DMOS used for this thesis 11

Figure 6: Equations used to calculate netOD from prescan and postscan 12

Figure 7:The path of a light ray traveling into a cylindrical dosimeter.. 14

Figure 8: Projection images used to adjust the RI of the matching fluid 14

Figure 9: Simulations of the edge artifact in various scanning conditions 15

Figure 10: The usable radius in dosimeter vs. RI of the matching fluid. 16

Figure 11: Schematic representation of the gamma analysis. 19

Figure 12: High-impact polystyrene phantom used for cuvette irradiations 26

Figure 13: Schematic showing the setup for the irradiation. A PRESAGE® dosimeter with a cavity filled with water is positioned in between solid water slabs 26

Figure 14: Reconstructed image of a slice in a cylindrical dosimeter and line profile. 29

Figure 15: Calibration curve for the two batches of PRESAGE® cuvettes, B1 and B2 31

Figure 16: A side view at the dosimeter with no plug inserted (left) and with plug inserted in the cavity (right). 32

Figure 17: Projections from postscans of (i) conventional method, (ii) plug method, (iii) fill-in method 2 days and (iv) 7 days after filling in the cavity. 33

Figure 18: Reconstruction images from the plug method (slices 20 and 30) containing severe artifacts due to the physical defect on the plug (slice 20) and air bubbles (slice 30). 33

Figure 19: Four ROI defined to calculate the mean signal and standard deviation in each reconstructions.......... 34

Figure 20: Outputs from change-point detection code for different RI-matching methods. The black line shows the average line profile, starting from the surface of the cavity and directed radially outward, into the dosimeter body. The red line shows where the code identified the change-point. Each index corresponds to a 0.5 mm distance.......... 36

Figure 21: Schematic of GMW Dipole Electromagnet 3472-70 (left) and photo of the electromagnet with the plexiglass phantom inserted between pole faces (right).......... 40

Figure 22: Design of the plexiglass phantom, consisting of a holder and different inserts to hold either cuvettes of film pieces.......... 41

Figure 23: Profile of the magnetic field supplied by the electromagnet at 49.8 V, 74.4 A, using 5 cm pole caps and a 3.5 cm pole gap.......... 42

Figure 24: (Top) Schematic of the irradiation setup with the electromagnet at extended SAD setup. The center of the magnet is located 300 cm from the gantry. (Bottom) Photo of the experiment setup with the cerrobend blocks placed in front of the electromagnet to collimate the beam. The original field is shown by the green light field.......... 43

Figure 25: Calibration curve for Gafchromic® EBT3 film used for the project.......... 46

Figure 26: Relative dose response of films irradiated in B = 0 and B = 1.5 T.......... 48

Figure 27: Relative dose response of PRESAGE® cuvettes irradiated in B = 0 and B = 1.5 T.......... 50

Figure 28: ABS plastic phantom and (left) setup for PRESAGE® dosimeter irradiation and (right) setup for film irradiation.......... 54

Figure 29: Side image of the setup for the experiment, shown without the phantom. The phantom is placed such that the dosimeter lies flat on the couch, with gantry at 90˚. The red diamond shows the position of the radiation field, which remains consistent, while the dosimeter is shifted for the second irradiation, creating different dose regions in the dosimeter.......... 55

Figure 30: The phantom containing the dosimeter on the treatment couch, positioned based on laser marks. After the first irradiation in one position (left), the phantom is shifted to create a high dose region (right)..55

Figure 31: Workflow for film-PRESAGE® comparison 58

Figure 32: A schematic showing the design and setup of the ABS plastic phantom parts (holder and insert) containing the dsoimeters. 59

Figure 33: (Left) Film and PRESAGE® images spatially registered and (right) the segment structure overlaid. Gamma analysis in 3D Slicer is performed only within the mask structure. 60

Figure 34: Gamma map produced from global (left) and local (mid) gamma analysis........................61

Figure 35: (i) Dose from the averaged film and PRESAGE® dosimeter 1 overlaid, (ii) dose from the averaged film and PRESAGE® dosimeter 2 overlaid, (iii) segment structure for gamma analysis overlaid, (iv) gamma map for averaged film vs. PRESAGE® dosimeter 1, [2] gamma map for averaged film vs. PRESAGE® dosimeter 2 62

Figure 36: Line profiles of averaged film, PRESAGE® dosimeters 1, and PRESAGE® dosimeter 2, taken along the same axis. 63

Figure 37: Illustration of n observations (y) broken into segments (x). 69

Figure 38: The reference and target matrix generated in Matlab. The square area in the upper left corner of the matrices were given fixed values of 0 and 1. 72

Figure 39: R code used to evaluate the effect of batch difference on the calibration curve. P-value is shown in red. With p >> 0.05, there is no interbatch variability observed..73

Figure 40: R-code used for the ANOVA analysis between film response in B = 0 and B = 1.5 T. The p-value is shown in red...74

Figure 41: R-code used for the ANOVA analysis between PRESAGE® response in B = 0 and B = 1.5 T. The p-value is shown in red. 76

List of Tables

Table 1: Gamma criteria used by IROC-Houston for credentialing institutions [6]. 19

Table 2: netOD values for all cuvettes. The reading for cuvette 2 in B1 (marked with *) was discarded due to a physical defect on the cuvette. 30

Table 3: Mean signal and signal-to-noise ratio over the four ROI, calculated for each RI-matching method. 35

Table 4: The thickness edge artifact (in mm) identified by the change-point detection code is tabulated for three methods in artifact-free slices. 37

Table 5: NetOD measured for each film pieces 47

Table 6: NetOD values obtained for each film irradiated in B = 0 and B = 1.5 T. 49

Table 7: NetOD values obtained for each PRESAGE® cuvette irradiated in B = 0 and B = 1.5 T. 51

Table 8: Local gamma analysis passing rates calculated with 5 %/ 3 mm gamma criteria, for averaged film vs. PRESAGE® dosimeter 1 and 2, with and without dose constraint of (D > 1 Gy). 62

Table 9: Results of gamma analysis for dataset 1 and 2. 72

Table 10: Input for the R-code shown in Figure 35, used to test for inter-batch variability in PRESAGE® 74

Table 11: Input for the R-code shown in Figure 36, used to test for magnetic field effect in film. 75

Table 12: Input for the R-code shown in Figure 37, used to test for magnetic field effect in PRESAGE®. 77

Chapter 1 – Introduction

1.1. Introduction to radiation therapy

With the capacity to deliver a highly conformal beam to the target volume, radiation therapy has become a popular cancer treatment method. In 2010, National Cancer Institute (NCI) reported that about half of all cancer patients are expected to undergo some type of radiation therapy over the course of their treatment (1). Among various types of radiation therapy, external-beam radiation therapy using high-energy photon beams produced by linear accelerators is widely used to treat tumors in a variety of tumor sites. With technological advances that enable precise placement and continuous modulation of radiation beam, modern linear accelerators are capable of delivering high dose to the target volume while sparing nearby healthy structures. The remaining challenge is to localize the tumor and to ensure that the tumor falls in the targeted area for each irradiation. The simplest way to do this is to use immobilization devices or to put external markers on the patient, such that the patient is aligned with the radiation beam in accordance with the treatment plan, every time the patient is on the table. However, the position of the internal organs is often not fully explained by the position of external markers due to factors such as internal motion in the patient and weight loss of the patient. Thus the use of external markers alone is not sufficient to ensure that the internal anatomy of the patient is aligned as planned.

The efforts to visualize the patient’s anatomy on the table at the time of treatment led to the development of image guided radiation therapy (IGRT). In IGRT using linear accelerators, on-board imaging (OBI) capacity allows imaging the patient just before delivering the radiation. Most on-board imaging modalities currently in the clinic use X-ray to generate images: some examples include projection images produced by megavoltage (MV) beams from the linear accelerator and projection images and cone-beam CT images produced by a kilovoltage (kV) unit added onto the linear accelerator. The images obtained from the OBI allow positioning the patient based on the anatomical structures and hence reduces the uncertainty in the location of the target.

1.2. Development of MRgRT

The feasibility of using magnetic resonance imaging (MRI) for radiation therapy treatment position verification is currently being investigated, leading to the development of MRI-guided radiation therapy (MRgRT). Compared to X-ray imaging, MRI offers a number of benefits. First, MRI does not use radiation to generate images and thus removes the concern for harmful effects from the imaging dose. This is beneficial especially for fractionated treatments, for which the imaging dose can accumulate to a significant level over the course of the treatment. MRI also offers superior soft tissue contrast, allowing the physician to delineate the target volume and surrounding structures more easily. Since MRI does not use radiation to produce images, it is also possible to image the patient during the treatment and to monitor the real-time location of the target volume. Functional imaging capacity in MRI also allows the assessment of treatment response, during and post-treatment, thus allowing the treatment to be adjusted based on the radiation response, providing a more personalized treatment for each patient.

Some MRgRT treatment machines have been designed and are already commercially available. Viewray (Viewray, Ohio, United States of America) produces the MRIdian system, which combines three ^{60}Co teletherapy heads to deliver radiation in a 0.35 T magnetic field. The MR-linac, which combines a linear accelerator with a closed-bore MRI scanner, was developed as a collaboration between UMC Utrecht (The Netherlands) and Elekta (Crawley, UK). In Figure 1, the sketch of the MR-linac is shown where a linear accelerator (Elekta) is mounted on a ring around the 1.5 T Philips (Best, The Netherlands) MRI system (2).

Despite the benefits of MR imaging, MRgRT faces some challenges to be resolved before reaching the full potential. A major concern is the change in the delivered dose distribution due to the strong magnetic field used for MR imaging. In radiation therapy, dose is mainly delivered by secondary electrons that carry the energy transferred from the initial beam. Secondary electrons are mostly forward peaked and deposit energy downstream, as they travel deeper into the patient, in

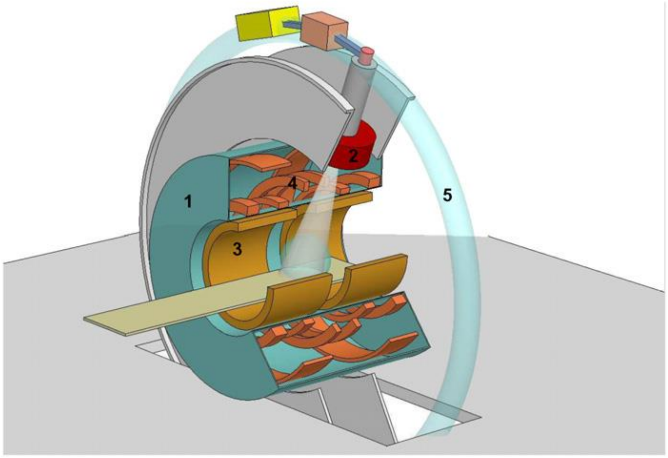

Figure 1: Sketch of the MR-linac system concept: (1) 1.5 T MRI, (2) 6MV linear accelerator; (3) split gradient coil, (4) super conducting coils, (5) low magnetic field toroid in the fringe field (2).

segments of straight lines. In the magnetic field, however, the path of the secondary electron is altered due to the Lorentz force. When the electron is generated in a dense medium and travels into a less dense medium, the electron is able to follow a circular path, back into the original medium. Due to the lack of the electronic equilibrium, dose is enhanced in the original medium near the interface. This phenomenon is referred to as the electron return effect (ERE) and has been shown to pose clinical concerns (3). Figure 2 shows how the trajectory of an electron traveling from one medium to the next is different in the absence and presence of the magnetic field, along with a clearer demonstration the ERE (4). In the Monte Carlo simulation and the film measurement by Raaijmakers *et al* (Figure 3), the ERE is observed to enhance dose at the interface by up to a factor of 1.3 ~ 1.4, over about 1 cm range (3).

The ERE is a clinical concern not only because it significantly enhances dose at the interface but also because the intensity and pattern of the ERE are dependent on various factors. These factors include the media comprising the interface, the shape and orientation of the interface, the strength of the magnetic field, and the energy of the beam. Investigations by Raaijmakers *et al* show that the dose can be enhanced up to 150 % over a range of up to 1 cm at the interface (4). Some measures such as using opposing beams have been shown to alleviate the ERE in relatively simple geometry (3, 5). However, because the ERE is dependent on a number of factors, it still remains a concern for the treatment of heterogeneous treatment sites and regions containing airways and cavities.

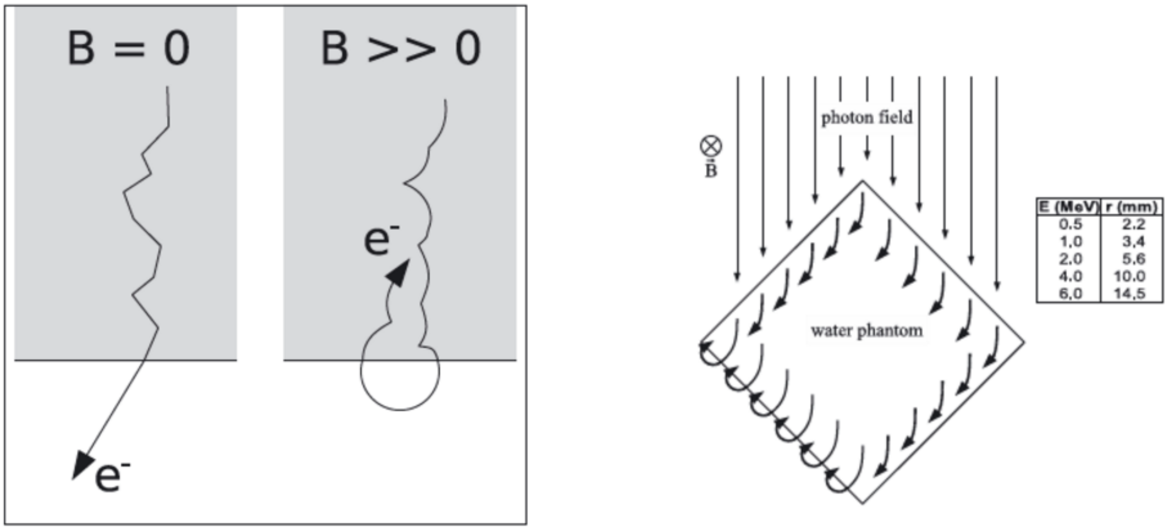

E (MeV)	r (mm)
0.5	2.2
1,0	3,4
2,0	5,6
4,0	10,0
6,0	14,5

Figure 2: (Left) An example of the trajectory of a secondary electron traveling in (L) zero and (R) finite magnetic field. In magnetic field, the electron travels back to the original medium (4). (Right) Schematic demonstration of how dose is enhanced at the left beam exit surface due to the ERE (4).

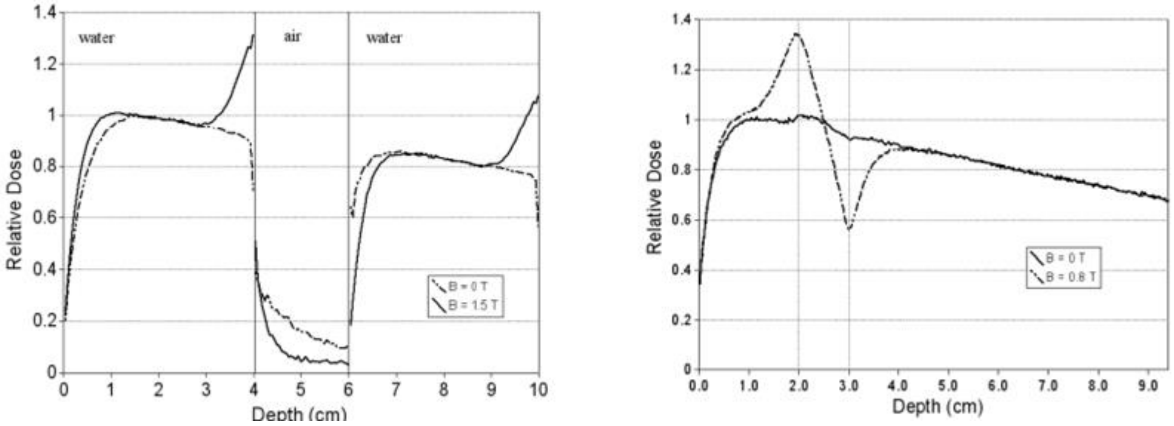

Figure 3: (Left) Monte-Carlo simulation result showing the dose profile along the central beam axis through water-air-water interface and (right) film measurement of the dose profile along the central beam axis through plastic-air-plastic interface (3).

1.3. Implication for the quality assurance (QA) of MRgRT equipment

1.3.1. 2D dosimetry and 3D dosimetry

Current conventional quality assurance (QA) procedures in radiation therapy usually relies on two-dimensional (2D) dosimetry, using film and point dosimeters to compare the measured dose to the planned dose in a few planes and points of interest. The Imaging and Radiation Oncology Core Houston (IROC-Houston) QA Center also uses 2D dosimetry with radiochromic film, to credential institutions to participate in clinical trials. In the credentialing process, IROC-Houston sends out an anthropomorphic QA phantom containing a target to the clinic that applied for credentialing. The clinic proceeds through its independent workflow in creating the treatment plan and irradiating the phantom, after which the phantom is sent back to IROC-Houston for analysis of the irradiated dosimeters. IROC-Houston uses the planar and point dosimeters that were located in the phantom to evaluate whether the delivered dose distribution agrees with the institution’s calculated treatment plan dose distribution.

In 2010, IROC-Houston reported that 20-30 % of credentialing attempts had failed for treatment sites such as head and neck (H&N), spine, and lung (6). A more recent report shows that even for irradiations performed since 2012, still a significant number of irradiations do not meet the passing criteria (7). Considering the fact that the delivered dose was evaluated only in a few planes, it can be readily expected that a more comprehensive investigation would reveal even more points where the delivered dose deviates or agrees with treatment plan. For MRgRT treatments, where the magnetic field is expected to change the delivered dose distribution in a complicated fashion over the irradiated volume, the need for a more thorough means of measuring the dose to perform a detailed comparison is emphasized.

As an effort to overcome the limited number of sampling points in 2D dosimetry, three-dimensional (3D) dosimeters have been developed to provide volumetric dose information. The materials commonly investigated are polymer gel, radiochromic gel, and radiochromic plastic (PRESAGE®) materials (8). Depending on the material and formulation, the 3D dosimeters can be read out using different read-out methods such as MRI, X-ray CT, and optical-CT. With the capacity to measure and compare volumetric dose distribution, 3D dosimetry has the potential to serve as an important complement or even a substitute of 2D dosimetry, if well investigated.

1.3.2. PRESAGE®

PRESAGE® is a radiochromic plastic material that was introduced in 2006 (8). It consists of an optically clear, firm polyurethane matrix doped with free radical initiators and leuco dye. For radical initiators and leuco dye, halocarbons and leucomalachite green (LMG), respectively, are commonly used. When irradiated, the radical initiators produce free radicals in the dosimeter, which oxidize the LMG into malachite green. This chemical change causes local optical density (OD) and color change inside the dosimeter, from colorless to dark green. The change in the OD is proportional to dose delivered and can be measured using a spectrophotometer, for cuvettes, and an optical-CT, for larger volumetric dosimeters. The dosimetry system using PRESAGE® and the optical-CT has been under further development since the first appearance in 2006 (9).

PRESAGE® offers a number of benefits that makes it an attractive option for 3D dosimetry. Consisting of polyurethane matrix, PRESAGE® is solid, thus able to retain its shape alone, and is insensitive to oxygen. This removes the need for any external casing, which is required for gel dosimeters, and allows PRESAGE® to be easily cast into a variety of shapes by using different molds and through careful machining. PRESAGE® dosimeters with embedded cavities and channels were shown to be suitable for brachytherapy applications (10-12), and the feasibility of 3D printing PRESAGE® into various shapes and making regions of varying density was also investigated (13). The firmness and oxygen insensitivity make PRESAGE® dosimeters easy to handle, allowing potential widespread use. Financially, compared to other dosimetry systems that use MRI or X-ray CT for analysis, the PRESAGE®-optical-CT system is more affordable and can be a more desirable option for small institutions and clinics.

The dosimetric properties of PRESAGE® dosimeters also make it suitable for various applications. Studies have reported linear dose response up to approximately 100 Gy, negligible energy dependence in 145 kVp to 18 MV region, and negligible dose-rate dependence for photon beams with dose rates from 100 cGy/min to 600 cGy/min (9, 14-17). Sakhalkar *et al* reported post-irradiation signal increase, but it was shown to have no effect for the relative dosimetry (16).

Because PRESAGE® is relatively new compared to other 3D dosimetry materials, investigations are still underway to optimize the formulation for different applications. The radiation response of each PRESAGE® dosimeter depends on the formulation and even on the batch of the material, so it is critical to test and validate the dosimeter's characteristics of interest, such as dose linearity and sensitivity, when working with each formulation. It is also important to ensure inter-batch and intra-batch consistency, if the dosimeters are produced in-house.

1.4. PRESAGE® dosimetry using Optical-CT system

When radiation is delivered to a PRESAGE® dosimeter, the conversion of LMG into malachite green causes local changes in the OD. This radiation-induced contrast is light-absorbing in nature, with the absorption peak around 633 nm. By using a visible light source that emits red light at the matching wavelength, the optical-CT produces 2D maps of optical attenuation coefficients in the dosimeter (18). The process and principles used in the process are very similar to how a clinical CT obtains 2D maps of X-ray attenuation coefficients in a patient. The OD of the dosimeter is measured using the optical-CT before (prescan) and after irradiation (postscan), and the net change in OD (netOD) is correlated to dose.

1.4.1. Optical-CT system

In 1996, Gore *et al* introduced the basic concepts of gel dosimetry using the optical-CT (19) . The optical-CT system essentially uses the same principles as a clinical X-ray CT, to obtain 2D maps of optical attenuation coefficients in the dosimeter. Although the optical-CT uses visual light rays instead of X-rays, the monochromatic light beam under narrow-beam conditions is also assumed to be attenuated exponentially according to the following equation:

$$I(x) = I_0 e^{-\int \mu(x,y)dy}$$

where $\mu(x, y)$ is the optical attenuation coefficient per unit length at a region inside the dosimeter, I_0 is the intensity of the light incident on the dosimeter, and $I(x)$ is the intensity of the light as it exits the dosimeter. The prototype optical-CT system suggested by Gore *et al* is shown in Figure 4. In this system, the narrow-beam condition is satisfied by using a point laser source, and the reference detector is used to measure the initial intensity of the beam. The beam is pointed perpendicularly into a tank that contains a rotating stage, on which the dosimeter is positioned. The dosimeter in the tank is immersed in a body of fluid (“matching fluid”), whose refractive index (RI) should ideally match

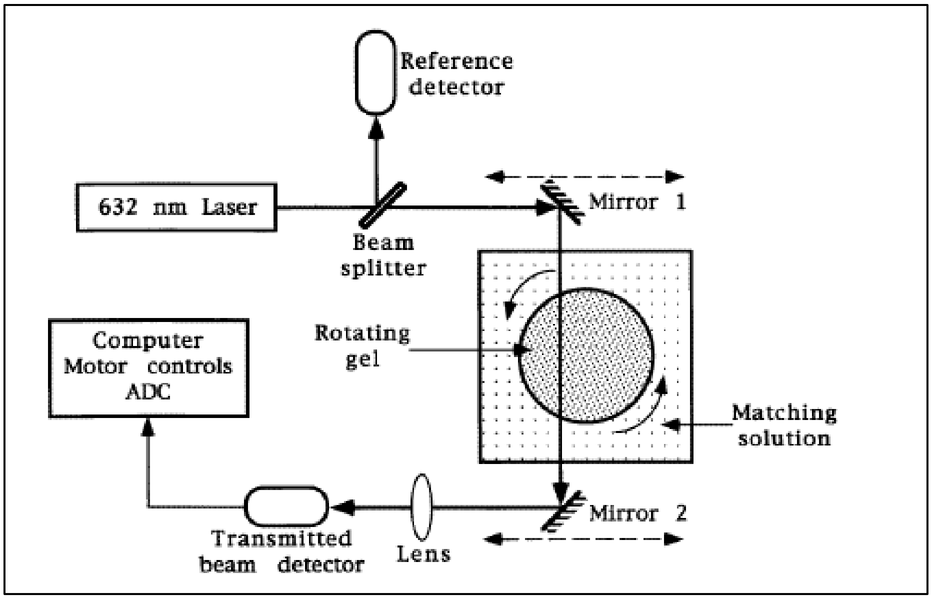

Figure 4: Design of the prototype optical-CT (19).

that of the dosimeter. This prevents the refraction of light rays at the fluid-dosimeter interface and suppresses the edge artifact, which degrades image quality in the optical-CT system. The edge artifact is further explained in Section 1.4.3. In the prototype optical-CT, the attenuation profile in one slice of the dosimeter is obtained by moving Mirror 1 and 2 along the tank wall. After one full projection is acquired, the stage mounting the dosimeter rotates, and the projection for the next angle is acquired. Repeating the process, the sinogram for one slice of dosimeter is be generated.

In order to obtain the netOD, the sinogram from the prescan is divided by the sinogram from the postscan, which is referred to as image subtraction. Then image reconstruction is performed, mostly using filtered back-projection. The final image is a 2D map of netOD in the dosimeter, which is related to the beam intensity by the following equation:

$$\Delta OD = -\Delta \log_{10}(\frac{I}{I_0})$$

where I is the measured intensity and I_0 is the initial intensity.

Constant investigations are underway to improve the image quality and optimize the workflow in optical-CT scanning. In 2015, De Deene *et al* (2015) proposed a dual-wavelength optical-CT system that removes the need for prescan (20). When scanning the dosimeter after irradiation, this system scans the dosimeter at one additional wavelength that is insensitive to the dose response. This method is expected to improve the quality of the PRESAGE®-optical-CT system by removing repositioning errors between the prescan and postscan.

1.4.2. Duke Mid-sized Optical-CT System (DMOS)

The prototype optical-CT that was shown in Section 1.4.1 had concerns for practical implementation because scanning the whole volume of the dosimeter using a point light source took a long time. This type of optical-CT was reported to take approximately 7 min to acquire the data to obtain an image of a single slice, with the total scan time accumulating up to several hours (21, 22). To overcome this drawback, the Duke Mid-sized Optical-CT System (DMOS) utilizes an LED light source with a diffuser to produce a broad-beam, which acquires the projection at one angle for all slices at once on a CCD camera. This accelerates the total acquisition time to 10-20 minutes. A pair of telecentric lens is placed on either side of the tank containing the dosimeter to ensure that the light rays travel parallel to the optical axis. The imaging lens can reject any stray or scattered light rays that deviate more than 0.1˚ from the original axis. The tank containing the dosimeter is placed between the lenses such that the walls facing the two lens are oriented perpendicular to the optical axis. The rotating stage on the bottom of the tank is connected to a motor that is controlled by a LabView-based data acquisition software, and the projections at different angles are obtained by rotating the dosimeter. Inside the tank, the dosimeter is immersed in the matching fluid. A schematic of the DMOS used throughout this thesis is shown in Figure 5.

In the DMOS system, there are some factors that may give rise to signals that are not

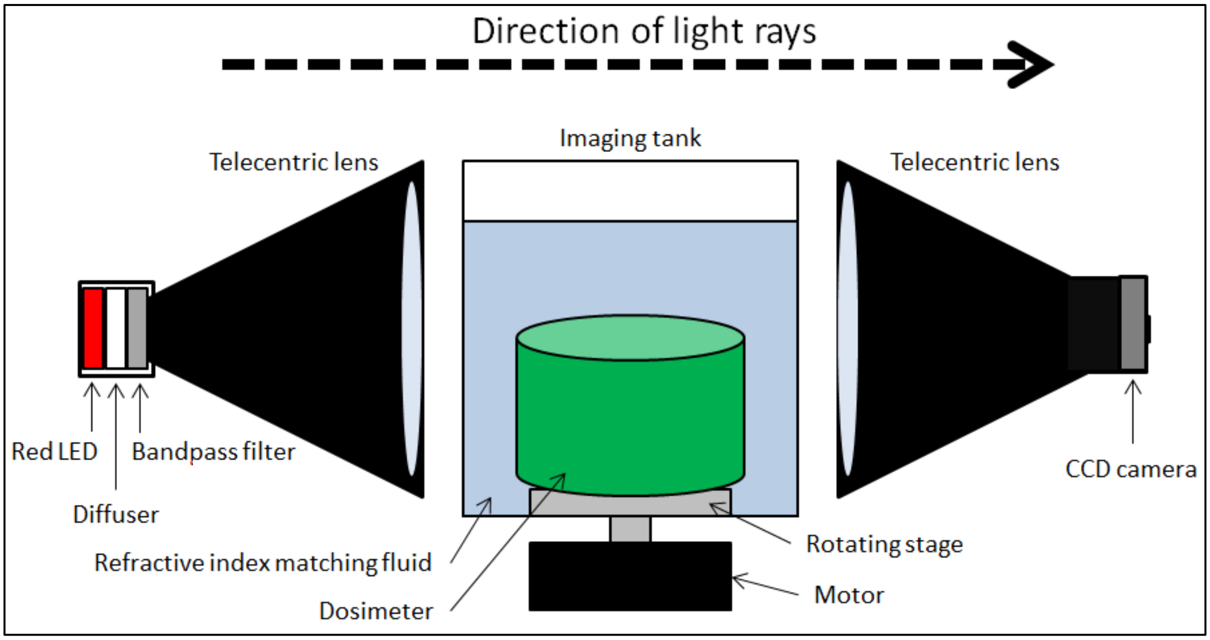

Figure 5: Schematic of the DMOS used for this thesis

representative of the dose delivered to the dosimeter. Scratches on the tank, nonuniformity in the light field, debris floating inside the tank, and swirling due to incomplete mixing of the matching fluid are some examples of the imperfections in the system that degrades the signal’s dose dependence. In order to correct for such imperfections, each projection image is corrected using a flood image, which is the average of 200 images taken with an empty tank. The images are also corrected using a dark image, which accounts for the dark current in the electronics. The dosimeter itself also may have factors that may give rise to signal that is not representative of the dose delivered. Some examples include impurities and air bubbles inside the dosimeter, scratches on the surface, and inherent signal due to thermal reaction or exposures to day light. The image subtraction using the prescan and postscan, to obtain the net change in OD, accounts for these dosimeter-related factors. Equations relevant to the correction and subtraction are as shown in Figure 6, with further details provided in Juang (2015) (23).

In order to relate the netOD with the dose delivered, a simple conversion can be performed using a linear calibration curve. To obtain the calibration curve, cuvettes of PRESAGE® are irradiated to different dose levels, and their OD are measured, typically using a spectrophotometer, before and after irradiation. The netOD is calculated by taking the difference between the OD measured at the prescan and that measured at postscan. However, the dimensions of the cuvettes are often set such that the path length through the dosimeter is unit length (1 cm), so this must be taken into account

$$I_1 = transmitted\ light\ intensity\ collected\ by\ camera$$

$$I_0 = incident\ light\ intensity$$

$$\left(\frac{I_1}{I_0}\right)_{pre} = \frac{prescan - dark_{pre}}{flood_{pre} - dark_{pre}}$$

Dark/flood correction for prescan image

$$\left(\frac{I_1}{I_0}\right)_{post} = \frac{prescan - dark_{post}}{flood_{post} - dark_{post}}$$

Dark/flood correction for postscan image

$$\ln\left(\frac{\left(\frac{I_1}{I_0}\right)_{pre}}{\left(\frac{I_1}{I_0}\right)_{post}}\right) = \ln\left(\frac{\mathrm{I}_1}{\mathrm{I}_0}\right)_{\mathrm{pre}} - \ln\left(\frac{\mathrm{I}_1}{\mathrm{I}_0}\right)_{\mathrm{post}} = -\Delta\ln\left(\frac{I_1}{I_0}\right)\ between\ pre/post$$

Image subtraction via sinogram division

$$\Delta OD = -\frac{\Delta\ln\left(\frac{I_1}{I_0}\right)}{\ln(10)} = -\Delta\log_{10}\left(\frac{I_1}{I_0}\right) between\ pre/post$$

Conversion to ΔOD

Figure 6: Equations used to calculate netOD from prescan and postscan

when converting a volumetric netOD read-out data from the optical-CT to dose, which have much smaller voxel sizes. The more popular way in obtaining dose information from a PRESAGE®-optical-CT system is to use PRESAGE® as a relative dosimeter, by scaling the PRESAGE® read-out to a known dose. Once the linearity of the formulation is confirmed using cuvettes, PRESAGE® reading can be scaled by picking one or more points with a reliable signal and then scaling the signal to the known dose at those points.

1.4.3. Edge artifact

PRESAGE® dosimetry using the optical-CT suffers from edge artifact, which refers to the loss of dose dependence of the signal at the edge of the dosimeter due to light refraction. When light rays travel through two media with different RIs, they are refracted away from the original direction, resulting in loss of signal at the detector. If the dosimeter contains regions with different RIs, the light rays may also be refracted inside the dosimeter, but the most pronounced effect is at the edge of the dosimeter, hence the name edge artifact. The greater the mismatch in the RI between the dosimeter and its surrounding, the greater the signal loss, resulting in a more severe artifact. Figure 7 shows a worst-case scenario in which a PRESAGE® dosimeter is surrounded by air (RI = 1), whose RI is very different from that of PRESAGE® (RI ~ 1.5). The light ray traveling into the dosimeter is badly refracted away from the original direction, according to Snell's Law (24).

In order to minimize the edge artifact, the dosimeter is scanned inside a bath of matching fluid, whose RI matches that of the dosimeter. The RI of the matching fluid is often manually manipulated by mixing fluids with different RIs. The RIs of the matching fluid and the dosimeter is matched by using a refractometer, by visually inspecting the projection images until the artifact at the dosimeter edge is minimized, or by combining the two methods. Figure 8 shows an example of a series of projection images that may be used to visually match the RI. The red arrow points to the image where the RI is well-matched.

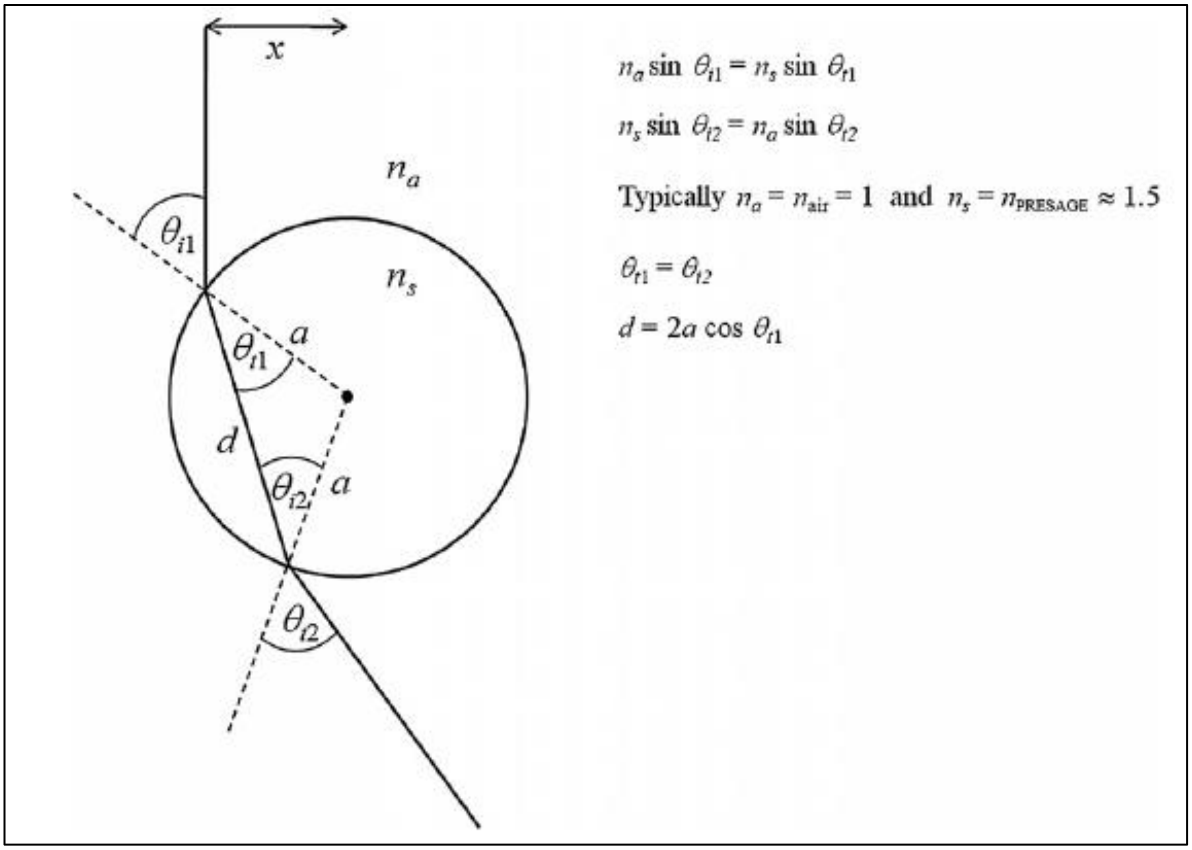

Figure 7: A schematic showing the path of a light ray traveling through a cylindrical dosimeter(viewed from the top). The light ray is refracted away from the original direction according to Snell's Law (24).

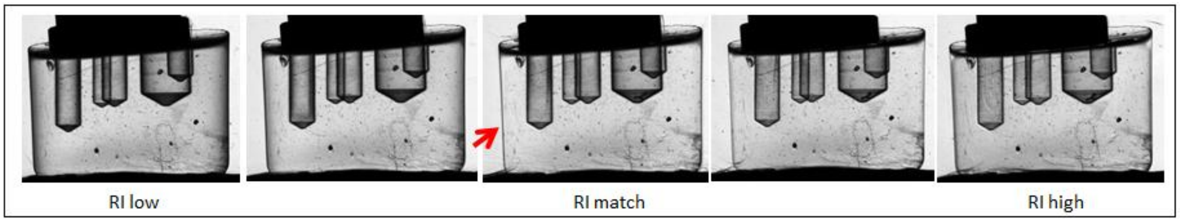

Figure 8: Projection images of a small dosimeter with vertical cavities in the matching fluid with varying RI. On the left, the RI of the matching fluid is lower than the RI of the dosimeter. Fluid with high RI is gradually mixed in until eventually the RI of the matching fluid is higher than the RI of the dosimeter in the last image.

Even with these measures, the edge artifact is so sensitive to any mismatch in the RI that it is nearly impossible to completely remove the edge artifact. In Figure 9, simulations by Doran *et al* (2012) effectively show how light rays imaging a cylindrical dosimeter travel when the dosimeter is in air, perfectly RI-matched matching fluid, and slightly mismatched matching fluid (24). Even with 0.3 % mismatch in the RI between the dosimeter and the matching fluid, several millimeters of edge artifact is observed in the projection profile. In 2015, Chisholm *et al* investigated the "dry-scanning method," which replaced the bath of matching fluid with a solid tank with a fixed RI at 1.5. The solid tank had a cylindrical cavity inside which a cylindrical PRESAGE® dosimeter was placed with a

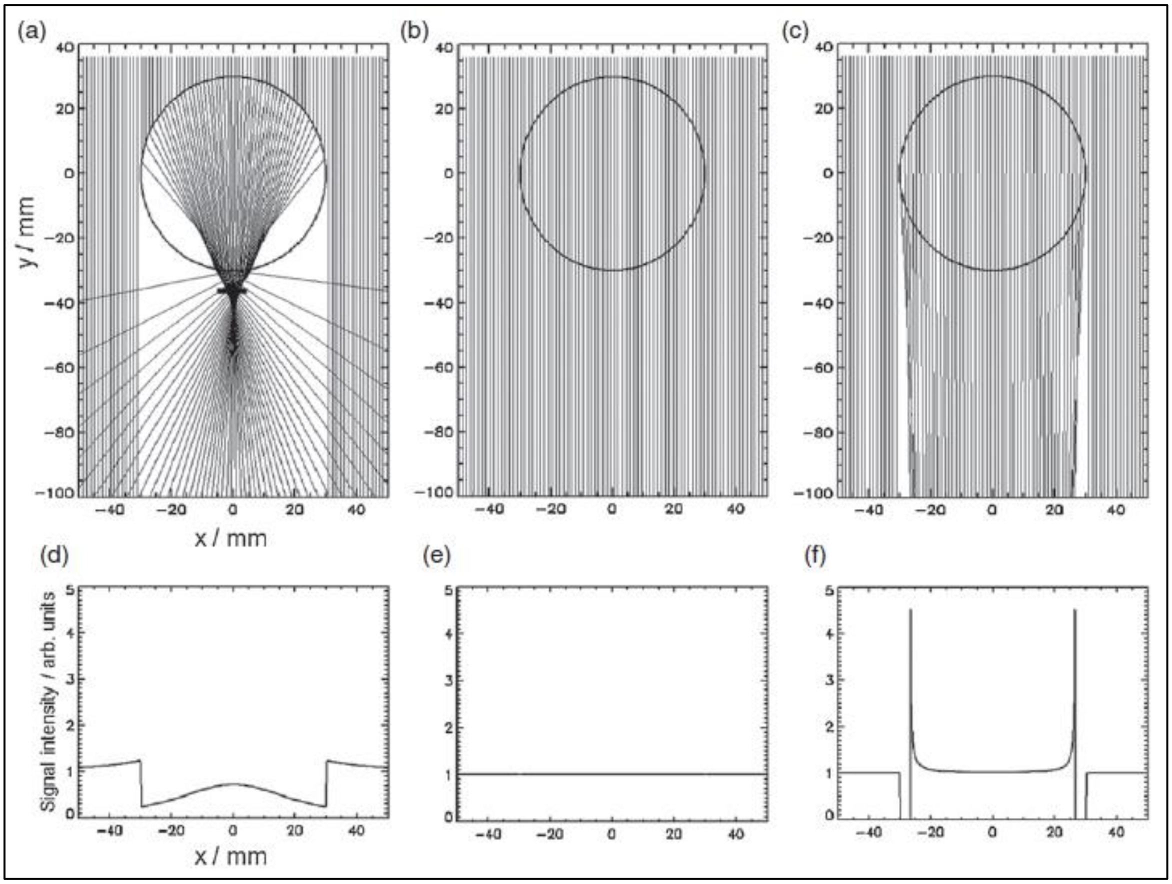

Figure 9: (a)-(c) Simulations by Doran *et al* (2012) of light rays imaging a slice of a cylindrical dosimeter and (d)-(f) the projections obtained. (a) The dosimeter is surrounded by air, (b) perfectly RI-matched matching fluid, and (c) matching fluid with a 0.03 % mismatch in the RI (24).

1 mm gap between the cavity surface and the dosimeter, and the gap was filled with matching fluid, whose RI was varied (25). Figure 10 shows the usable radius in the dosimeter plotted against the RI of the matching fluid, with each curve corresponding to a different PRESAGE® dosimeter with a unique RI. For any dosimeter, a sharp peak in the usable radius curve was observed, which implied that the edge artifact was highly sensitive to the RIs of the dosimeter and the matching fluid.

Conventionally, studies using PRESAGE® dosimeters have excluded the regions of edge artifact from the analysis. The severity of the edge artifact varied for each study, but anywhere from the outer 3 mm to 8 mm rim of the dosimeter had been excluded from the analysis (26-28) . There have been efforts to correct for the edge artifact during the reconstruction process, but further investigation is needed for a more widespread and practical implementation (29, 30) of these methods.

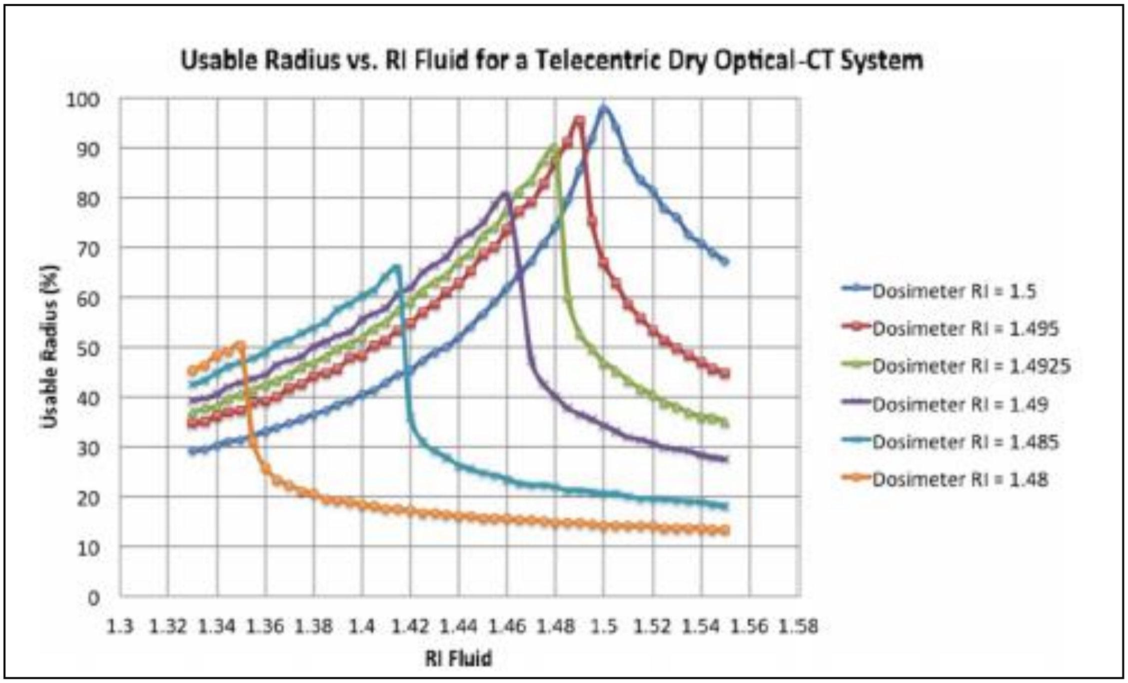

Figure 10: The usable radius in dosimeter plotted against the RI of the matching fluid, each curve for one dosimeter with a fixed RI (25).

1.5. Dosimeters in magnetic field

In order to use dosimeters as QA tools in magnetic field, it is crucial to understand how the magnetic field affects the response of the dosimeters. There have been relatively few investigations on how a strong magnetic field affects different dosimeters. In 2009, Meijsing *et al* reported the magnetic field effects on Farmer NE2571 ionization chamber. The study consisted of two parts—GEANT4 Monte Carlo simulation and experiments using the Farmer NE2571 ionization chamber in the magnetic field produced by an electromagnet. Depending on the orientation of the ion chamber and the strength of the magnetic field varying from 0 to 1.2 T, the response of the ion chamber varied 10-15 % (31). The effect of the magnetic field on thermoluminescent dosimeter (TLD), optically stimulated luminescent dosimeter (OSLD), Gafchromic® EBT3 film, and PRESAGE® had also been investigated (32). The conventional 2D dosimetry tools (TLD, OSLD, EBT3) were shown to have no significant magnetic field effects, while the results for PRESAGE® showed some under-response. The study also suggested that testing for magnetic field effects in PRESAGE® would require an investigation with a more well-defined experiment plan.

1.6. Gamma analysis

The gamma analysis is a well-established method commonly used to compare the agreement between two different dose distributions (33). In IROC-Houston's credentialing process, the gamma analysis is used to evaluate the ability of the clinics to deliver the dose as planned. This is done by comparing the dose distribution measured by radiochromic film and point dosimeters (TLD/OSLD) to the treatment plan, using the gamma analysis. In the clinic, the gamma analysis is also widely used in patient QA for intensity-modulated radiation therapy (patient IMRT QA), where the dose distribution planned for a patient is delivered to and measured by a phantom containing radiation detectors, and the agreement between the measured dose and the planned calculated dose is evaluated using the gamma analysis.

The gamma analysis compares two dose distributions by calculating the gamma index for each data point in the reference distribution. The gamma index is calculated based on two criteria—dose difference (DF) and distance-to-agreement (DTA). For a point in the reference distribution r_r receiving dose D_r, the dose difference criterion (ΔD_M) and the DTA criterion (Δd_M) jointly establish an ellipsoid of acceptance as can be seen in Figure 11. Typical values used for ΔD_M and Δd_M are 5 ~ 7 % and 3 ~ 5 mm, respectively (6). The dose difference criteria can be defined as a percentage of D_r (local gamma) or a fixed value (global gamma) such as the prescription dose or maximum dose in the plan. For each data point r_r in the reference volume, the spatial and dose information of the points in the evaluated dose volume ($\vec{r_c}, D_c$) are used to calculate the gamma index, which is defined as the following:

$$\Gamma_r(r_c, D_c) = \min(\sqrt{\frac{\Delta r^2}{\Delta d_M^2} + \frac{\Delta D^2}{\Delta D_M^2}})$$

where $\Delta r = \vec{r_r} - \vec{r_c}$ is the distance between the reference and evaluated point, and ΔD is the dose difference. The gamma index for the reference data point is, as stated in the equation, the minimum gamma value obtained for r_r. If the gamma index is equal to or smaller than 1, the data point “passes” the gamma test.

The passing fraction, or the passing rate, is calculated as the number of passing points divided by the number of points queried for analysis. The passing rate is commonly used as the single quantity representing the agreement between reference and compared dose distributions. The threshold for the gamma passing rate in the credentialing process at IROC-Houston is 85 % for varying gamma criteria for different treatment sites (Table 1). In research, the gamma analysis is often used to evaluate the performance of new dosimeters against established dosimeters, a treatment plan, or Monte Carlo simulations.

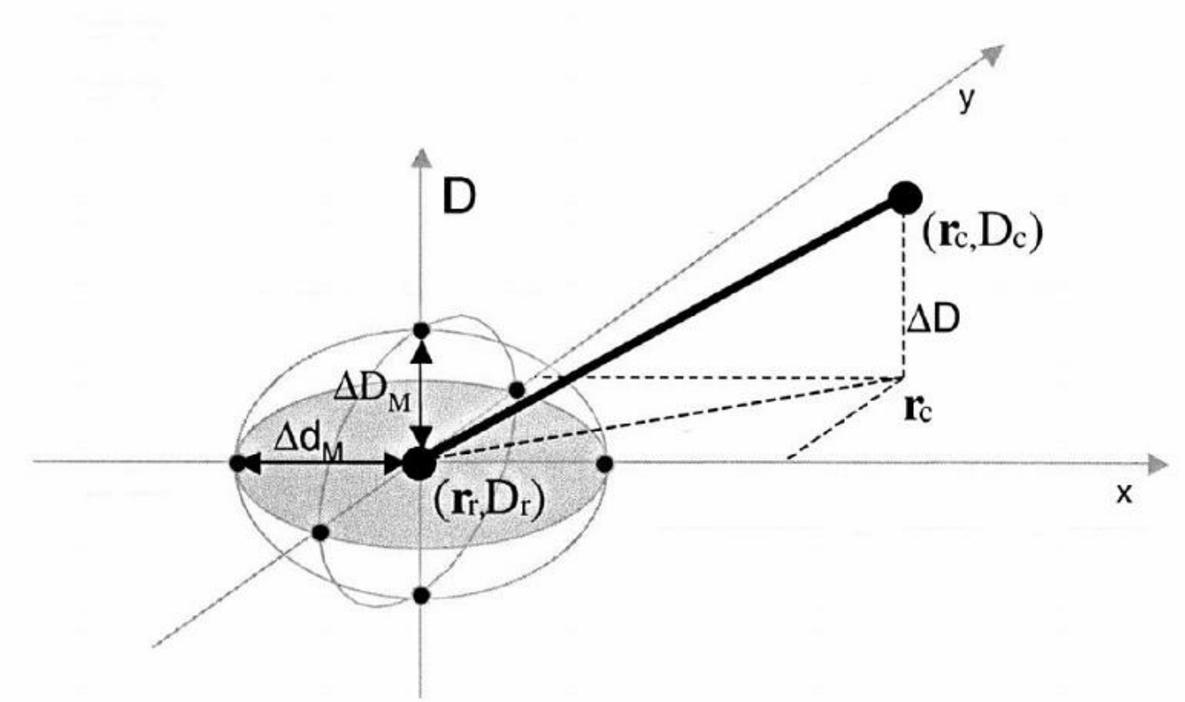

Figure 11: Schematic showing the quantities used for the calculation of the gamma index for point $\vec{r_r}$. The acceptance criteria is shown as an ellipsoid around the origin, defined by the two principal axes of length ΔD_M and Δd_M (34).

Head and Neck	Prostate	Spine	Lung	Liver
7 %/4 mm	7 %/4 mm	5 %/3 mm	5 %/5 mm	7 %/4 mm

Table 1: Gamma criteria used by IROC-Houston for credentialing institutions (6).

1.7. Validity of the PRESAGE®-optical-CT system

A number of studies have shown the reliability of the PRESAGE®-optical-CT system for practical applications of 3D dosimetry for simple and complex photon beams. In 2006, Guo *et al* evaluated the performance of PRESAGE® dosimetry for a simple 5-beam open-field treatment. The agreement among the PRESAGE®-optical-CT system, film dosimetry system using Gafchromic® EBT film, and treatment planning system (TPS) was evaluated. The measurement from the PRESAGE® system agreed well with the commissioned ECLIPSE® TPS and even better with film measurement at 4 % dose difference and 4 mm distance-to-agreement (DTA) gamma criteria. Due to the edge artifact, the outer rim of the PRESAGE® dosimeter, corresponding to nearly 10 % of the radius of the dosimeter, was excluded from the analysis (14). In 2008, Oldham *et al* demonstrated a high agreement of the PRESAGE® system with ECLIPSE® TPS for an intensity modulated radiation therapy (IMRT) plan using 11 field coplanar beams with planning target volumes (PTVs) and an organ-at-risk (OAR). Excluding the region of edge artifact, the pass rate was 96 % at 3 %/3 mm gamma criteria (27). Even including the region of edge artifact, the PRESAGE® system showed a performance similar to that of the film dosimetry system. Using the same gamma criteria, the pass rate for PRESAGE® versus TPS and EBT versus TPS were 91.4 % and 94.0 % respectively. Sakhalkar and Sterling *et al* showed that for IMRT irradiation of the Radiologic Physics Center (RPC) H&N phantom, the EBT film, PRESAGE®, and Eclipse agreed with each other with passing rates over 98 % (16). The gamma criteria used were 4 %/3 mm, and 4 mm near the edge of the PRESAGE® dosimeter was excluded from the analysis due to the edge artifact. In 2011, Thomas and Newton *et al* commissioned the PRESAGE®-optical-CT system. In this study, normalized dose distribution (NDD) was used as the metric for dose comparison. The NDD is a metric similar to the gamma index, except the passing values vary from -1 to +1, and the points with lower dose than the reference can be distinguished from the points with higher dose than the reference. Excluding the region of edge artifact, the PRESAGE® system showed 97.9 % agreement with the treatment plan for a four-field-box treatment at 3 % / 3 mm (28). In 2013, Iqbal *et al* also used the gamma criteria of 3 %/3 mm to show that for anthropomorphic breast phantom irradiations, EBT2 film, PRESAGE®, and Pinnacle TPS agreed well with each other (35).

1.8. General problem area

In order to take the full advantage of MRgRT, the change in the dose distribution due to the magnetic field needs to be closely monitored. If PRESAGE® dosimetry is proven feasible and reliable for MRgRT, it will provide a rigorous means to closely monitor the volumetric dose distribution in the area where the dose distribution is expected to be most affected by the magnetic field. In particular, the ability to measure the ERE will further provide benefits for estimating the dose distribution in MRgRT treatment of heterogeneous treatment sites containing structures such as the lung, trachea, and esophagus and for MR-guided brachytherapy, which inevitably involves body cavities and thus is prone to clinical problems posed by the ERE.

The accuracy of PRESAGE® dosimetry in the magnetic field can be evaluated by comparing the dose distribution measured by PRESAGE® dosimeters to Monte Carlo simulation or to the dose distribution measured by another independent dosimetry system. If comparing to an independent dosimetry system, the performance of the independent system needs to be proven reliable in the magnetic field, or the effect of the magnetic field on the independent system needs to be fully characterized.

1.9. Hypothesis and Specific Aims

The hypothesis for this thesis is that the dose distribution delivered in the presence of the magnetic field can be measured with PRESAGE® dosimeters to 5 %/3 mm agreement with that measured by film. For this project, the Gafchromic® EBT3 film was considered the gold standard for comparison because the performance of EBT3 was shown to be unaffected by the magnetic field in

2015 (32). Since the study is relatively new, however, this thesis included a section where the effect of the magnetic field on EBT3 is independently investigated.

The 5 %/3 mm gamma criteria was selected with consideration. For IMRT QA, 3 %/3 mm is used to evaluate the goodness of radiation delivery. The IMRT QA uses these tight gamma criteria because it uses detectors with small uncertainties and is carried out using a rather homogenous phantom. At IROC-Houston, the gamma criteria used for the credentialing process are more generous, varying from 5 %/3 mm to 7 %/4 mm depending on the treatment site. The generosity in the gamma criteria is due to the higher level of challenge in delivering the plan to a heterogeneous, anthropomorphic phantom and also due to the uncertainty in the dosimeters used. Compared to IMRT QA, which mostly makes relative dose comparison, IROC-Houston uses absolute dose comparison, which also makes it more challenging to achieve comparable pass rates at the same gamma criteria.

The 5 %/3 mm gamma criteria used for this project acknowledged two factors: (1) PRESAGE® is a material under development and thus has bigger uncertainties than the dosimeters used for IMRT QA, and (2) the dose distribution delivered to the dosimeter was expected to have a certain level of complexity due to the magnetic field effects and ERE. On the other hand, the gamma criteria was not relaxed further because PRESAGE® had been shown to make reliable measurements, and the irradiation was not expected to be as challenging as irradiating an anthropomorphic phantom.

This thesis is divided into three specific aims (SA):

Specific Aim 1 (SA1): Modify optical-CT scanning protocol to improve the PRESAGE® measurement in the vicinity of interfaces

Measurement of the ERE requires that a dosimeter be able to measure dose at the material-air interface. Through this aim, measures to improve the reliability of PRESAGE® measurement at the dosimeter-matching-fluid interface were investigated.

Specific Aim 2 (SA2): Assess the effect of the magnetic field on the response of EBT3 and PRESAGE® dosimeter

The response of EBT3 was tested for magnetic field effects in order to determine whether it would be suitable as the standard for evaluating the performance of the PRESAGE® system in the magnetic field. The response of PRESAGE® was also investigated with and without the magnetic field to understand how PRESAGE® response is affected by the magnetic field.

Specific Aim 3 (SA 3): Measure the ERE with PRESAGE® dosimeters and compare with film measurements

Dose measurement in the magnetic field using PRESAGE® dosimeters was compared against 2D measurements using EBT3, which was considered the standard for the scope of this thesis. The region of comparison included the region affected by the ERE to evaluate whether PRESAGE® can practically perform well as a QA tool in MRgRT.

Chapter 2 - Specific Aim 1

2.1. Rationale

In order to measure the ERE, the dosimeter used must be able to provide reliable measurement at the edge of the dosimeter, since the ERE is expected to enhance the dose at the dosimeter-air interface. Dosimetry using PRESAGE® dosimeters suffers from the edge artifact, which severely degrades dose dependence in the signal at the edge of the dosimeter. In this section, three methods are compared in their effectiveness in reducing the edge artifact.

Another challenge that is addressed in this section is the lack of a systematic method to identify the region of edge artifact. Conventionally, the region of edge artifact was determined by visually inspecting dose distributions or profiles. This way of defining the edge artifact is vulnerable to subjectivity and can be inconsistent even for a single observer. In order to compare the effectiveness of different methods in reducing the edge artifact, a systematic method was developed to exclude observer bias in defining the region of edge artifact.

2.2. Methods

2.2.1. Verifying dose response of in-house made PRESAGE® dosimeters

The PRESAGE® dosimeters used throughout this thesis were produced in-house. As a spot-check for the linearity in dose response and inter-batch consistency of the in-house-made dosimeters, dose response curves were generated and compared for two separate batches of in-house-made PRESAGE® (B1 and B2).

The two batches of PRESAGE® were prepared in semi-microcuvettes and irradiated using Elekta VERSA linear accelerator. A semi-microcuvette is essentially the same as a regular cuvette (1 cm x 1 cm x 4 cm), except that it has a smaller filling volume. For simplicity in this thesis, PRESAGE® prepared in a semi-microcuvette is be referred to as a cuvette.

For each cuvette irradiation, one cuvette was placed in the center of a square cutout in a high-impact polystyrene phantom. The experiment cuvette was placed in the cutout along with three dummy cuvettes to provide scatter equilibrium in the surrounding, and only the experiment cuvette was switched out for the subsequent irradiation (Figure 12). The polystyrene phantom was placed in between slabs of solid water to provide 1.5 cm buildup and 9 cm backscatter to the center of the cuvette. The cuvettes were irradiated to 0.5, 1, 3, 5, 7, 9, and 11 Gy, with 10 cm x 10 cm field size and 100 cm source-to-surface distance (SSD). Since the linearity of PRESAGE® dose response is well-known, one cuvette irradiated to each dose level was considered sufficient. To assure uniform dose delivery, each cuvette was flipped upside-down, halfway into each irradiation. The uncertainty in PRESAGE® response for both batches was evaluated at a single dose level by irradiating three cuvettes to 9 Gy. The optical density (OD) of the cuvettes was measured once after the irradiation, using a GENESYS™ 10S UV-Vis Spectrophotometer. Following the realistic workflow and timeline of the irradiation for a volumetric dosimeter, the measurement was performed 2 hours post-irradiation. The net optical density (netOD) was obtained by taking the difference between the OD of irradiated cuvettes and the OD of an unirradiated cuvette. The unirradiated cuvette was produced from the same batch as the irradiated cuvettes and handled identically, such that the subtraction resulted in the netOD change due to the irradiation only. The difference in sensitivity (ΔOD/Gy/cm) between B1 and B2 was evaluated using R-Statistical Software.

2.2.2. Methods to reduce the edge artifact

A short cylindrical PRESAGE® dosimeter was produced with a coaxial cylindrical cavity, around which the edge artifact was measured. The dosimeter was positioned in between 10 cm solid water slabs and was irradiated once with the gantry at 0^0, 100cm SSD, to deliver about 4 Gy to the center of the dosimeter. The cavity in the dosimeter was filled with water during irradiation to deliver a dose distribution that was as smooth and continuous as possible around the cavity. The schematic of the irradiation is shown in Figure 13.

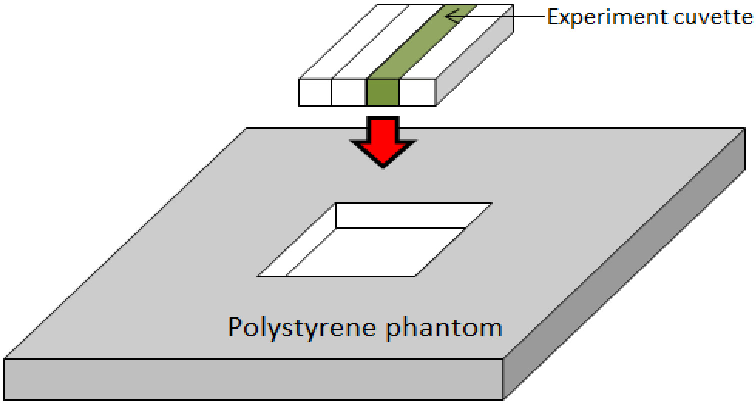

Figure 12: High-impact polystyrene phantom containing three dummy PRESAGE® cuvettes and one experiment cuvette.

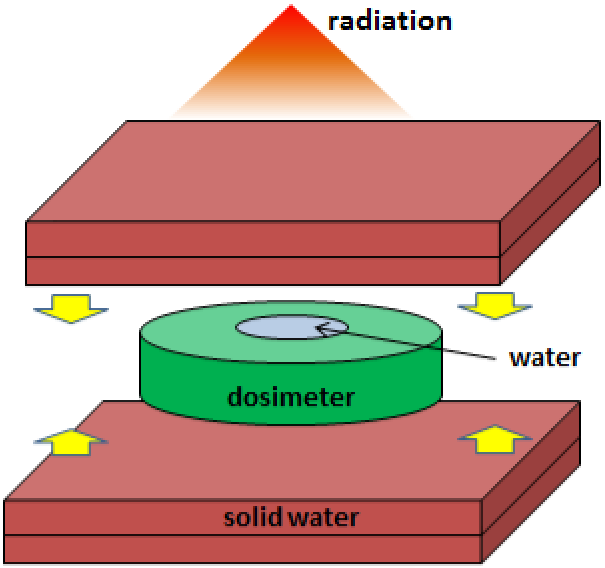

Figure 13: Schematic showing the setup for the irradiation. A PRESAGE® dosimeter with a cavity filled with water is positioned in between solid water slabs and is irradiated.

In the process of scanning the dosimeter, three methods were used to reduce the edge artifact at the surface of the cavity in the dosimeter. These methods are referred to as “RI-matching methods,” since all three methods attempted to reduce the edge artifact at the cavity surface of the dosimeter by closely matching the RI of the dosimeter with that of the material inside the cavity. First, the dosimeter was scanned using the conventional method, using only the matching fluid for both the prescan and postscan. The RI of the matching fluid was carefully adjusted to match that of the dosimeter by using a refractometer and visual inspection of real-time projection images as the RI was adjusted. For the second method, the dosimeter was scanned with a plug inserted into the cavity, for both the prescan and postscan. The plug was consisted of the same material as the dosimeter and was designed to tightly fit into the cavity. This is referred to as the “plug method.” In the third method, the dosimeter was prescanned in the matching fluid. After the irradiation, the cavity of the dosimeter was filled up with the same PRESAGE® material before postscan. This method is referred to as the “fill-in method.” The postscan was performed two days and seven days after filling in the cavity to investigate the effect of allowing extra time for the fill-in material to cure. For this method, it was acknowledged that the reconstruction would not show much improvement, if at all, in the level of edge artifact at the cavity surface, because the prescan and postscan were not performed using the same RI-matching method. Thus, the purpose of the fill-in method was to investigate mainly the projection images at the postscan and to study whether using the same PRESAGE® material to match the RI at the dosimeter edge, with zero air gap, would reduce the edge artifact in the projections.

2.2.3. Determining the region of edge artifact

In order to determine the severity of the edge artifact in different RI-matching methods in an observer-independent way and to quantitatively compare the level of edge artifact among the methods, a statistical time-series method called the “change-point detection method” was used. This time series analysis method models a nonstationary time series that can be segmented into blocks of different processes in time. The motivation for using this method was that a line profile taken through a dosimeter resembles a time-series data in a way, except the dose distribution is sampled at different spatial locations, not at different time points. Further description on the time series theory can be found in Appendix A. The code for the analysis was developed by the collaborators: Ting Fung Ma[1] and Chun Yip Yau[2], in a form that could be used in R-statistical software.

Figure 14 shows a slice from the optical-CT reconstruction of an unirradiated cylindrical dosimeter with a coaxial cylindrical cavity. Since the geometry of the dosimeter and the dose distribution is symmetric about the center of the cavity, line profiles taken at different angles (shown as red dotted lines) through the center of the cavity shared similar features, in that the edges of the dosimeter were distinguished by noticeable peaks, and the signal inside the dosimeter was relatively uniform. For the dosimeter irradiated as in Figure 13, the dose distribution was expected to be isotropic about the cylindrical axis of the dosimeter. Consequently, by taking multiple line profiles through the center and by using them as the input to the change-point detection code, the code was able to find the average thickness of the edge artifact in a reconstruction. For this project, 6 different line profiles were used for each RI-matching method.

Since the purpose of this specific aim was to evaluate the severity of the edge artifact at the cavity edge, the line profiles were truncated to start at the inner surface of the cavity and sample radially outward into the dosimeter body. Dose was sampled at every 0.5 mm interval. By converting the spatial information for each data point into the distance from the origin of the line profile, the line profiles were converted into a form that was appropriate for times series analysis.

---

[1] Census and Statistics Department, the Government of the HKSAR, Wan Chai, Hong Kong. Email: rtfma@censtatd.gov.hk.

[2] Department of Statistics, the Chinese University of Hong Kong, Shatin, Hong Kong. Email: cyyau@sta.cuhk.edu.hk

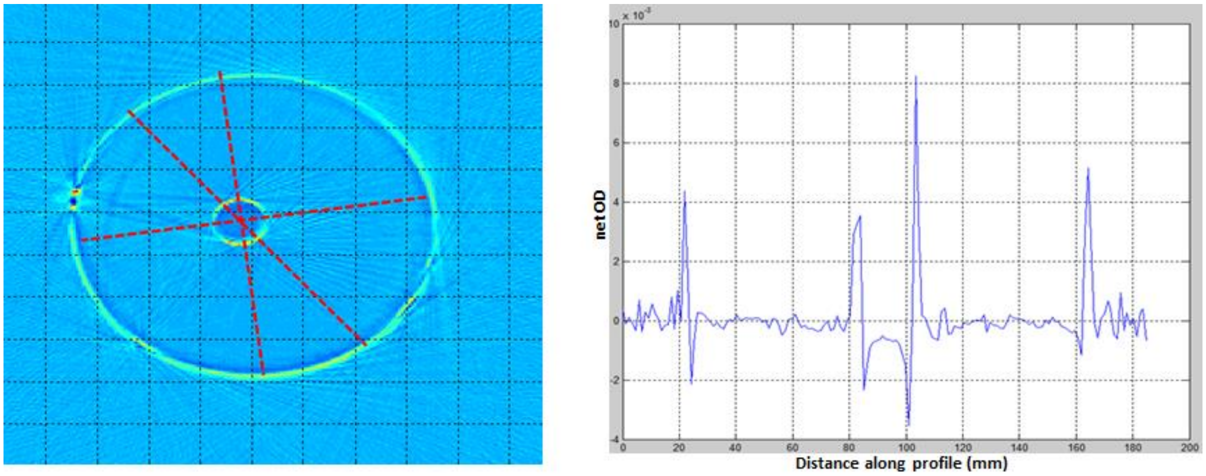

Figure 14: Reconstructed image of a slice in a cylindrical dosimeter with a cavity in the middle (left) and a typical line profile through the center of the cavity (right). Multiple line profiles can be taken at different angles, as can be seen by the red dotted lines.

2.3. Results

2.3.1. Verifying dose response of in-house made PRESAGE® dosimeters

Table 2 shows the netOD values obtained for each cuvette. Among the data obtained for B1, the reading for 0.5 Gy was discarded due to a physical defect on the surface of the cuvette. The uncertainty, calculated as the percentage of the sample standard deviation in the signal at 9 Gy divided by the average signal at 9 Gy, was 1-3%, depending on formulation. Figure 15 shows the

B1			B2		
cuvette#	Dose (Gy)	netOD (cm^{-1})	cuvette#	Dose (Gy)	netOD (cm^{-1})
1	0	0	1	0	0
2*	0.5	0.0237	2	0.5	0.0031
3	1	0.008	3	1	0.0069
4	3	0.0258	4	3	0.026
5	5	0.0452	5	5	0.0452
6	7	0.0598	6	7	0.0623
7	9	0.0794	7	9	0.0823
8	9	0.0835	8	9	0.0824
9	9	0.0843	9	9	0.0837
10	11	0.0999	10	11	0.1019
Standard deviation (std) at 9Gy:		0.00263	Standard deviation (std) at 9Gy:		0.00078
Uncertainty (%):		3.19	Uncertainty (%):		0.94

Table 2: netOD values for all cuvettes. The reading for cuvette 2 in B1 (marked with *) was discarded due to a physical defect on the cuvette.

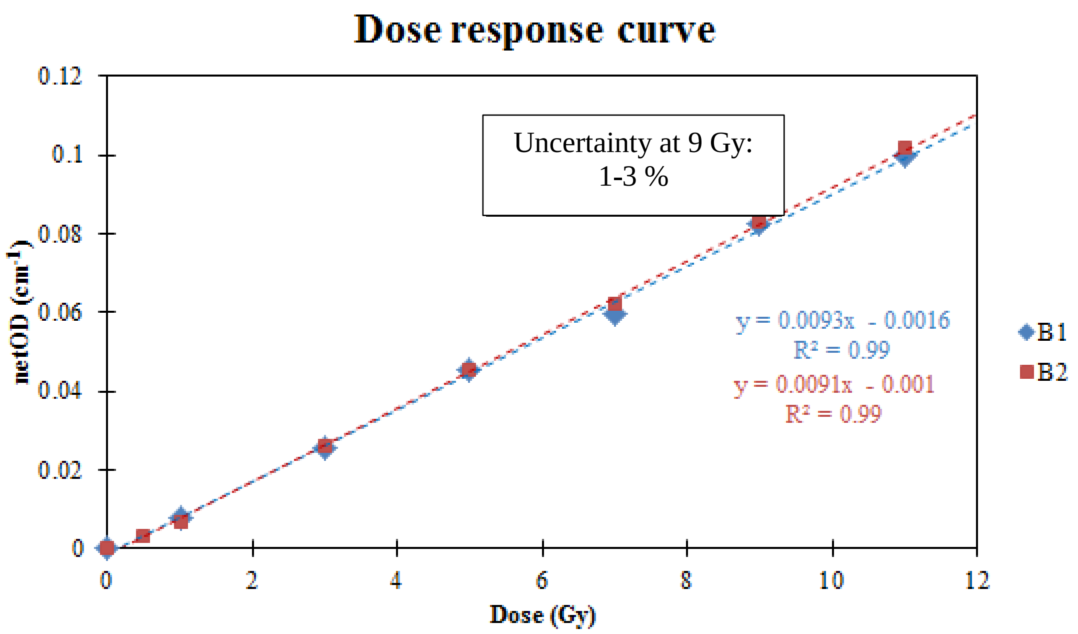

Figure 15: Calibration curve for the two batches of PRESAGE® cuvettes, B1 and B2

dose response curves for B1 and B2, along with the respective linear fit models. The plot visually demonstrates the equivalency in the dose response of the two batches. The effect of the batch difference on the slope of the calibration curve (sensitivity) was tested in R-statistical software, and the effect was shown to be insignificant with a p-value of 0.3752. The code written in R-statistical software to test for the difference in the two response curves and its input file can be found in Appendix C (Figure 39, Table 10).

2.3.2. Methods to reduce the edge artifact

Figure 16 shows the photos of the dosimeter taken with and without the plug inserted. A noticeable change in the diminished visibility of the cavity surface was observed when the plug was in place, implying a good match of optical properties and a promising RI match between the plug and the dosimeter. Figure 17 shows raw projection images from the postscans of each method. In the projection image obtained at the postscan of the plug method as shown in Figure 17 (ii), it was observed that the tight fit between the plug and the cavity surface had resulted in scratches on the surface of the plug and air bubbles caught between the plug and the cavity surface. The physical defects and air bubbles resulted in a significant amount of image artifact in most reconstructed slices for the plug method. Figure 18 shows the reconstructed slices from the plug method that contain severe artifacts from the imperfections, which made the plug method inappropriate for use. The black arrow on the projection images in Figure 17 point to where the plug method was least affected by the defects or air bubbles, but even in these areas, the plug method failed to show much difference in the level of edge artifact from the conventional method shown in Figure 17 (i).

Figure 17 (iii) and (iv) show the projection images from the postscan of fill-in method, performed two days and seven days after filling in the cavity, respectively. The first postscan was performed two days after filling in the cavity when the fill-in material had cured physically firm enough to be scanned in the optical-CT. For this scan, the fill-in method failed to demonstrate much

Figure 16: A side view at the dosimeter with no plug inserted (left) and with plug inserted in the cavity (right).

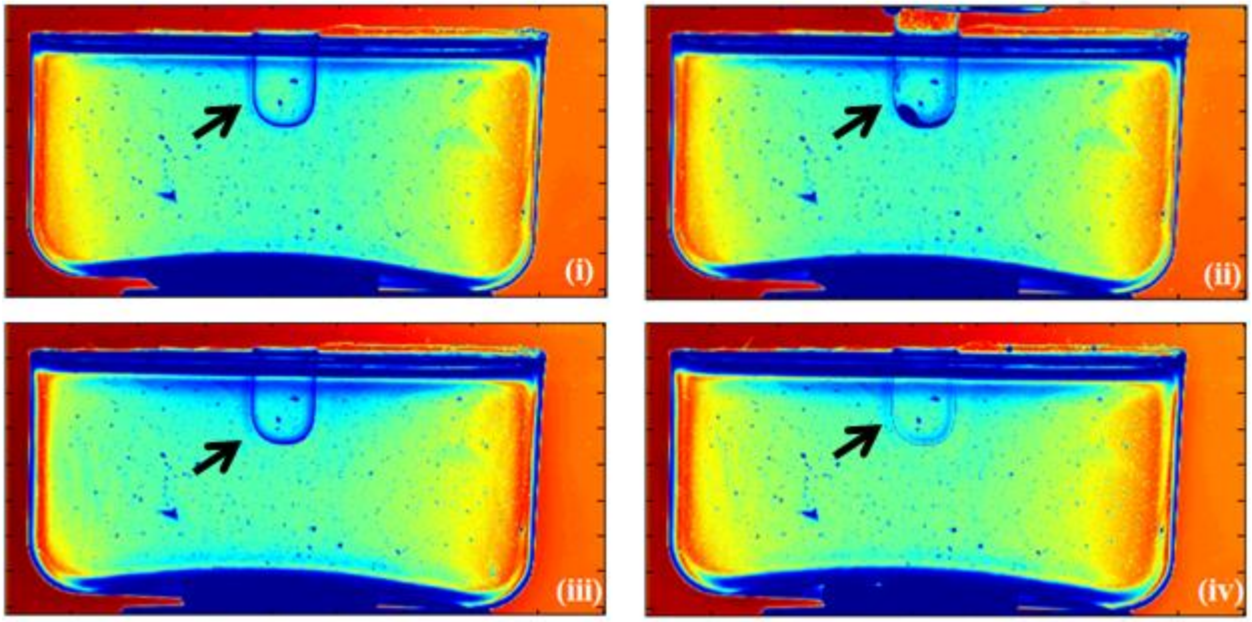

Figure 17: Projections from postscans of (i) conventional method, (ii) plug method, (iii) fill-in method 2 days and (iv) 7 days after filling in the cavity.

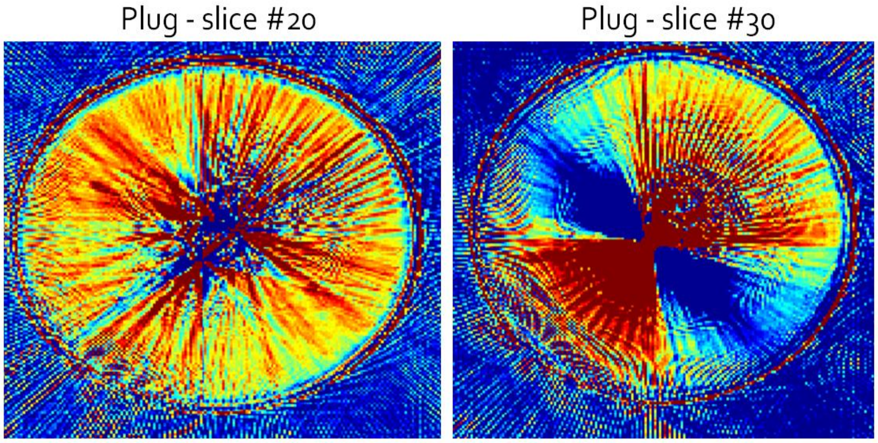

Figure 18: Reconstruction images from the plug method (slices 20 and 30) containing severe artifacts due to the physical defect on the plug (slice 20) and air bubbles (slice 30).

improvement in the level of edge artifact. However, in the projection image taken seven days after filling in the cavity, a big improvement in the edge artifact was observed at the cavity surface. The purpose of the extra time was to allow more time for the fill-in material to fully cure and for the optical property of the fill-in material to settle, and the projection image proved that the extra time made a significant difference. However, while filling in the cavity and waiting for the fill-in material to cure, the dosimeter had spent a long time in room temperature. Due to the time spent in non-refrigerated environment, the dose signal in the fill-in scans had been severely deteriorated. To evaluate the amount of signal deterioration, four regions of interest (ROI) were defined in each of the reconstructions, and the mean and standard deviation in the signal were calculated (Figure 19). Compared to the conventional method, the fill-in method performed two days and seven days after filling in the cavity showed 8 % and 25% decrease in the mean signal, respectively. The signal-to-noise ratio (SNR), calculated as the mean signal divided by the standard deviation, had deteriorated 49 % and 69 %, respectively (Table 3).

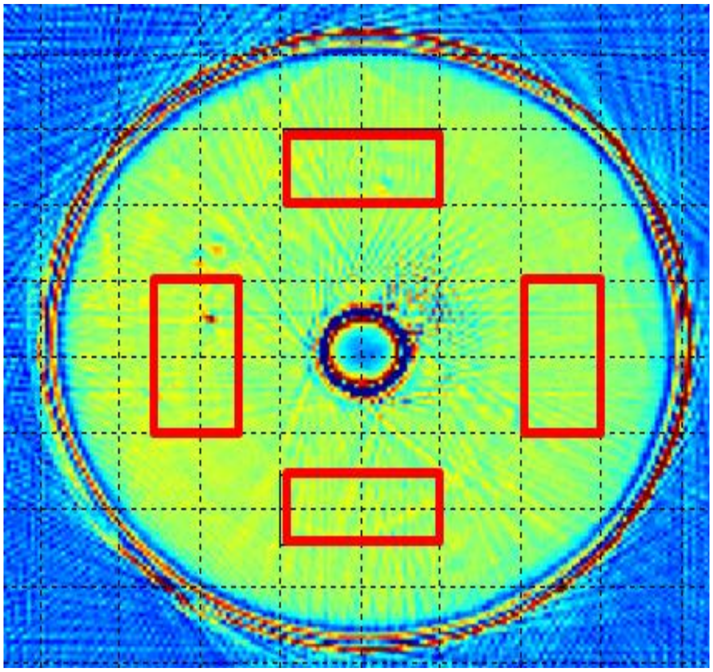

Figure 19: Four ROI defined to calculate the mean signal and standard deviation in each reconstructions

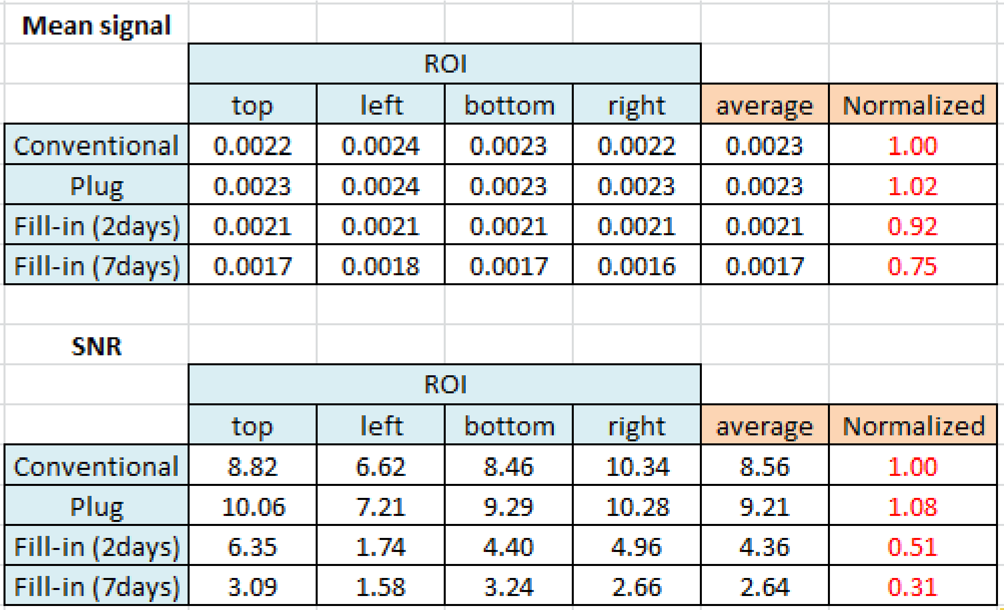

Mean signal

	ROI					
	top	left	bottom	right	average	Normalized
Conventional	0.0022	0.0024	0.0023	0.0022	0.0023	1.00
Plug	0.0023	0.0024	0.0023	0.0023	0.0023	1.02
Fill-in (2days)	0.0021	0.0021	0.0021	0.0021	0.0021	0.92
Fill-in (7days)	0.0017	0.0018	0.0017	0.0016	0.0017	0.75

SNR

	ROI					
	top	left	bottom	right	average	Normalized
Conventional	8.82	6.62	8.46	10.34	8.56	1.00
Plug	10.06	7.21	9.29	10.28	9.21	1.08
Fill-in (2days)	6.35	1.74	4.40	4.96	4.36	0.51
Fill-in (7days)	3.09	1.58	3.24	2.66	2.64	0.31

Table 3: Mean signal and signal-to-noise ratio over the four ROI, calculated for each RI-matching method.

2.3.3. Determining the region of edge artifact using change-point detection code

Error! Reference source not found. shows some results from the change-point detection ode in identifying the change-point in the line profiles of different RI-matching methods. For the image reconstruction process in fill-in method, the prescan was obtained using the matching fluid only, as described in Section 2.2.2. For the postscan, the images obtained two days after filling in the cavity were used because although the postscan performed seven days after filling in the cavity had less edge artifact, image quality was much worse due to the deteriorated signal as shown in Section 2.3.2.

In the outputs from the change-point detection code (Figure 20), the vertical and horizontal axes corresponded to the strength of the signal and the distance along the line profile, respectively. The distance between each index on the horizontal axis corresponded to a 0.5 mm distance. The code displayed the average line profile that was used as input in black and denoted the region that it identified as the change-point from edge artifact to regular dose signal as a red vertical line. It can be observed that the code successfully identified the region of edge artifact in a way that human observers would agree with visual inspection as well.

In the reconstructed images, slices 27, 28, and 29 contained the minimum artifact for all RI-matching methods. The change-point detection code was applied to these slices to determine the severity of the edge artifact in multiple slices for each RI-matching method. Table 4 shows the thickness of the edge artifact as identified by code. The conventional, plug, and fill-in method was shown to have edge artifact thickness of 0.5-1.5 mm, 1-2.5 mm, and 1.5-2.5 mm, respectively. The difference among the methods was small, but the conventional method consistently showed the lowest level of edge artifact in all slices.

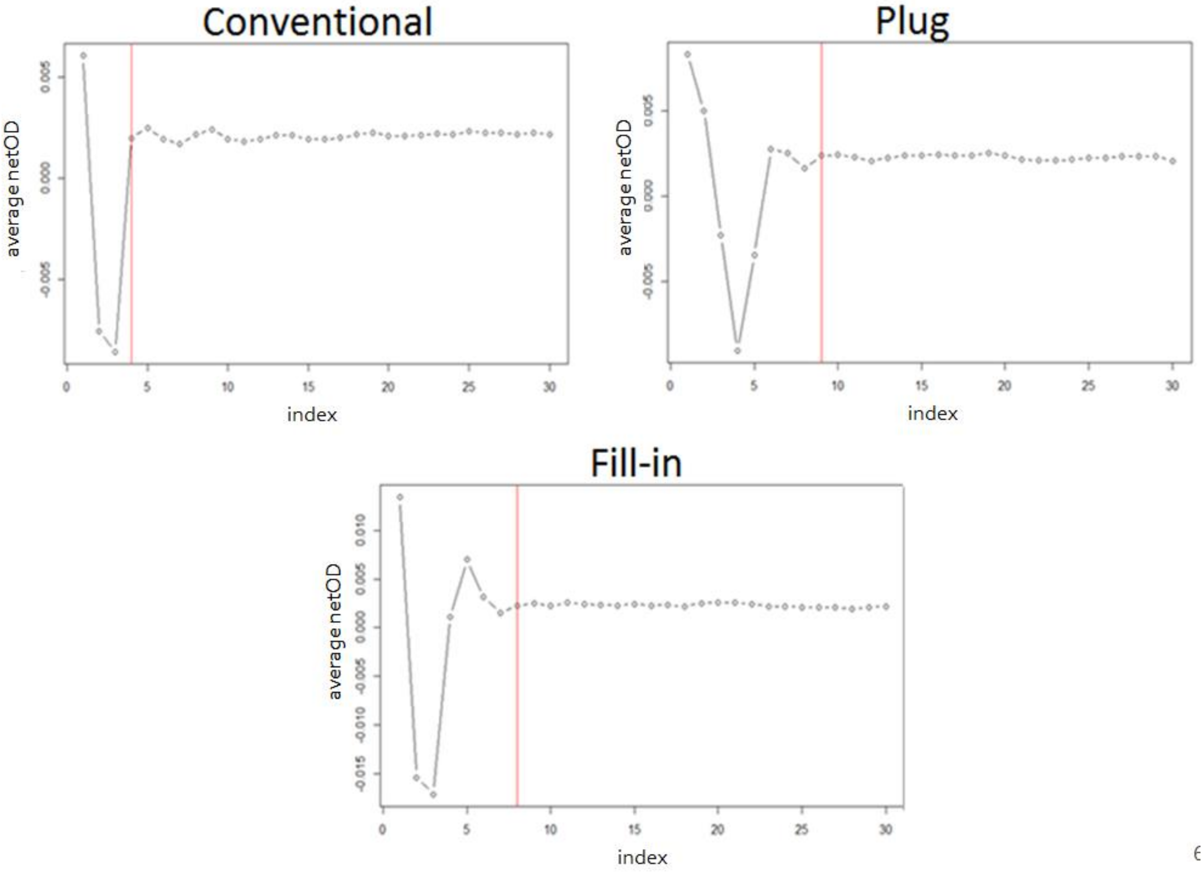
Conventional

Plug

Fill-in

Figure 20: Outputs from change-point detection code for different RI-matching methods. The black line shows the average line profile, starting from the surface of the cavity and directed

radially outward, into the dosimeter body. The red line shows where the code identified the change-point. Each index corresponds to a 0.5 mm distance.

	Slice 27	Slice 28	Slice 29
Conventional	0.5	1.5	1
Plug	2.5	1.5	1
Fill-in	2.5	2	1.5

Table 4: The thickness edge artifact (in mm) identified by the change-point detection code is tabulated for three methods in artifact-free slices.

2.4. Discussion

With 1-3 % uncertainty, the in-house made PRESAGE® formulation provided a reasonable SNR at 9 Gy and higher, which was comparable to the uncertainty in other dosimeters. EBT3 film and TLD were shown to exhibit 1-2 % and ±2 % uncertainty, while OSLD showed 3-4 % uncertainty at 95 % confidence level (36-38). For applications such as IMRT QA, where the dose involved is lower, this formulation of PRESAGE® would need to be altered to increase sensitivity. For this thesis, where there was no limit on the dose, this formulation was used while noting that a desirable level of SNR, comparable to other dosimeters, would be achieved at higher doses around 9 Gy.

From the projection images in Figure 17, it was evident that the fill-in method could be promising if allowed adequate time for the fill-in material to fully cure. However, two drawbacks exist in applying this method: (1) the fill-in cannot be undone, and (2) the time required for the fill-in material to cure results in signal deterioration. The fact that the fill-in cannot be undone is a problem for the experiments simulating the irradiation of airways or for brachytherapy applications, where the cavity needs to be emptied to contain air. In this case, the cavity in the dosimeter should be filled in for prescan, emptied for irradiation, and filled in again for postscan, since the scans need to be performed in identical conditions for image subtraction to work. However, during the curing process, bonds are formed between the fill-in material and the cavity surface, making it impossible to empty the cavity once the material cures. Efforts have been made to modify the PRESAGE®-optical-CT system to remove the need for prescan (20), and if this system succeeds, the fill-in method will provide a means to reduce the edge artifact. Even for such system, however, the issue of signal and SNR deterioration, while waiting for the fill-in material to fully cure, need to be addressed.

The plug method also failed to show any improvement over the conventional method. The failure is mostly attributed to the additional artifacts arising from the air bubbles and defects caused on the surface of the plug and the cavity due to friction. The small defects caused due to the friction may not be visible in the projection images, but when reconstructed, they cause severe streaking artifacts around the cavity.

Consequently, the conventional method was used to scan volumetric PRESAGE® dosimeters throughout this thesis. It is worthwhile to note that less than 2 mm thickness of the edge artifact was achieved using the conventional method. This result emphasized the importance of careful RI matching of the matching fluid in optical-CT scanning and also showed that PRESAGE® dosimeters could capture most of the ERE when testing the main hypothesis of the thesis.

Chapter 3 - Specific Aim 2

3.1. Rationale

This specific aim served as a preliminary step for the main experiment in SA 3. In SA 3, the quality of PRESAGE® dosimetry in magnetic field was to be evaluated by comparing the PRESAGE® measurements in the region of the ERE to radiochromic film measurements. The comparison to film measurement could be only be justified after showing that film could be used as a standard to evaluate the performance of another dosimeter in the magnetic field—that film dosimetry is reliable in magnetic field. From the recent literature, Gafchromic® EBT3 film was shown to be unaffected by the magnetic field (32). In this specific aim, the magnetic field effect on EBT3 was re-investigated, in order to demonstrate that EBT3 could be used as the standard for evaluating PRESAGE® performance in magnetic field.

In order to utilize PRESAGE® dosimeters for the quality assurance of MRgRT equipment in the future, it is also crucial to understand how the magnetic field affects PRESAGE® response. A recent literature suggested that the response of PRESAGE® is changed by the magnetic field, but no follow-up studies were performed to reproduce or further support the result (32). As a part of this specific aim, magnetic field effect on PRESAGE® was independently investigated in a well-defined setup.

3.2. Methods

3.2.1. Setup for irradiations involving magnetic field

For all experiments involving the magnetic field, radiation was delivered using an Elekta VERSA linear accelerator, and the magnetic field was provided by GMW Dipole Electromagnet 3472-70. Figure 21 shows the schematic of the front view at the electromagnet, along with a photo of

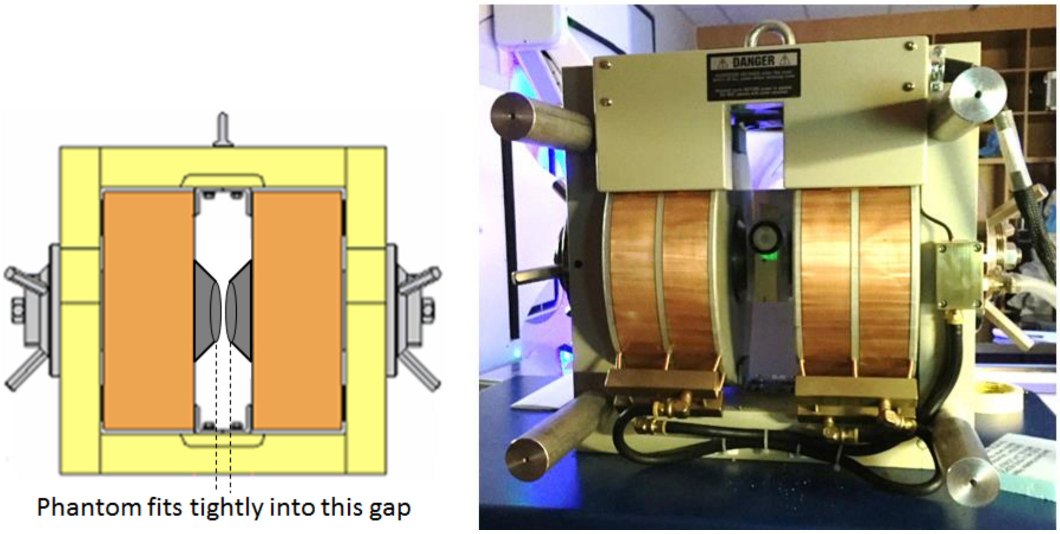

Figure 21: Schematic of GMW Dipole Electromagnet 3472-70 (left) and photo of the electromagnet with the plexiglass phantom inserted between pole faces (right).

the electromagnet with a plexiglass (acrylic) phantom inserted in between the pole caps. The magnetic field is formed between the circular faces of the pole caps, shown as gray pieces near the center of the electromagnet schematic. All dosimeters irradiated in the electromagnet were contained in a plexiglass phantom that was designed to hold the center of the dosimeters at mid-way between the pole caps (Figure 22). The phantom consisted of a holder piece that fit tightly between the pole caps to remain fixed in position, and an insert piece that allowed switching out the dosimeters and ensured consistent dosimeter positioning for all irradiations. The phantom also served to provide scatter medium around the dosimeters to provide 5 cm depth to the center of the dosimeters, such that the dose delivered to the central region of the dosimeters was not affected by the shift in the field or the ERE due to the magnetic field.

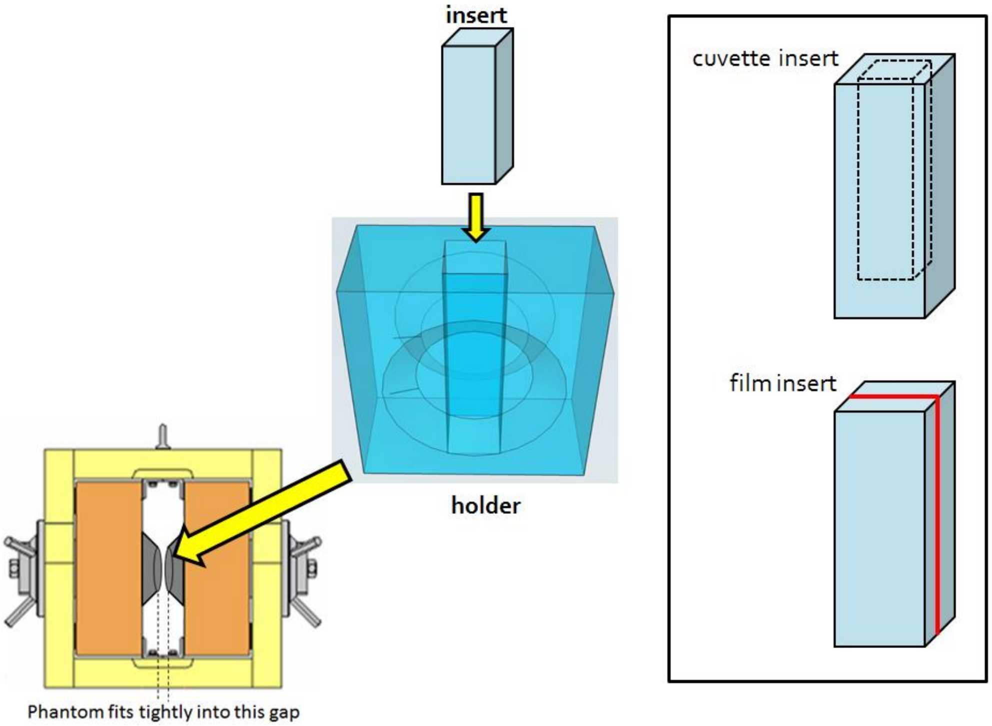

Figure 22: Design of the plexiglass phantom, consisting of a holder and different inserts to hold either cuvettes or film pieces.

The strength of the magnetic field could be adjusted by changing the parameters of the electromagnet such as the current, the distance between the pole faces (pole gap), and the diameter of the pole caps. For this thesis, to provide an environment that is as similar as possible to the clinical MRgRT equipment, the parameters of the electromagnet was set to provide a 1.5 T magnetic field at mid-way between the pole caps. The parameters used to achieve 1.5 T were 49.8 V, 74.4 A, 5 cm pole caps and a 3.5 cm pole gap. This condition is referred to as B = 1 5 T. For all irradiations done in zero magnetic field (B = 0) to compare the response to B = 1.5 T irradiations, only the power of the electromagnet was turned off while all other setup conditions remained the same.

Prior to all measurements, the strength of the magnetic field along the axis mid-way between the pole faces was measured. The measured magnetic field profile across the pole face is shown in Figure 23. In the central 3-4 centimeter region, the electromagnet was able to provide a constant magnetic field with less than 10 % change in the strength of the magnetic field. .

In order to prevent any electronic interference or magnetic coupling between the linear accelerator and the electromagnet, the electromagnet was positioned approximately 2 m from the isocenter with the gantry at 90°. The source-to-surface distance (SSD) to the phantom was 295 cm, with 5 cm depth to the dosimeters located at the center of the electromagnet pole caps. This is referred to as an extended source-to-axis distance (SAD) setup of 300 cm. The collimator setting used was 5 cm x 5 cm, and cerrobend blocks were set up in front of the electromagnet to collimate the field further to a 2 cm x 4 cm field. The additional collimation ensured that the radiation beam was delivered only to the part of the phantom containing the dosimeters while avoiding the electronics in the electromagnet (Figure 24).

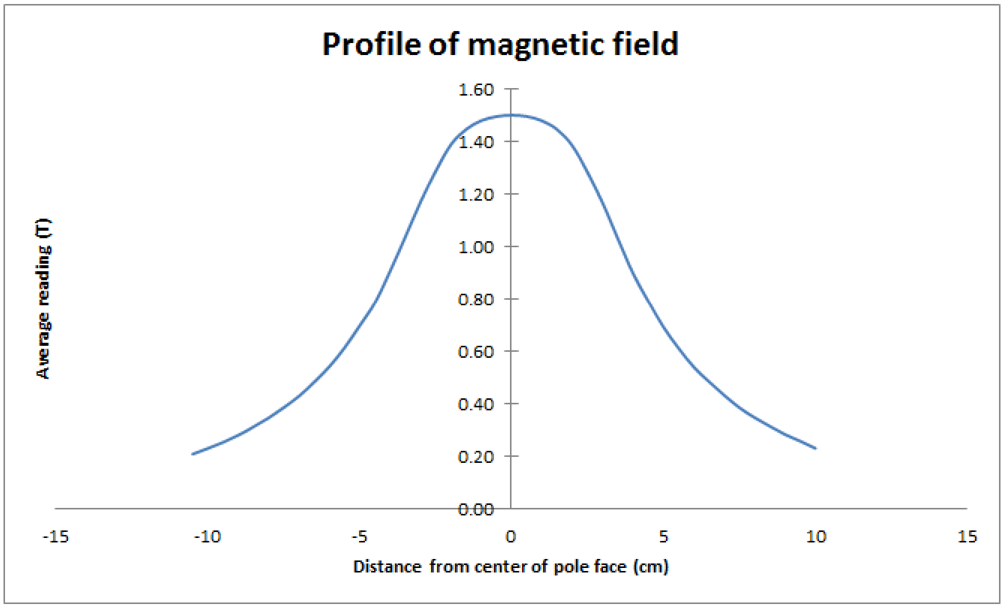

Figure 23: Profile of the magnetic field supplied by the electromagnet at 49.8 V, 74.4 A, using 5 cm pole caps and a 3.5 cm pole gap.

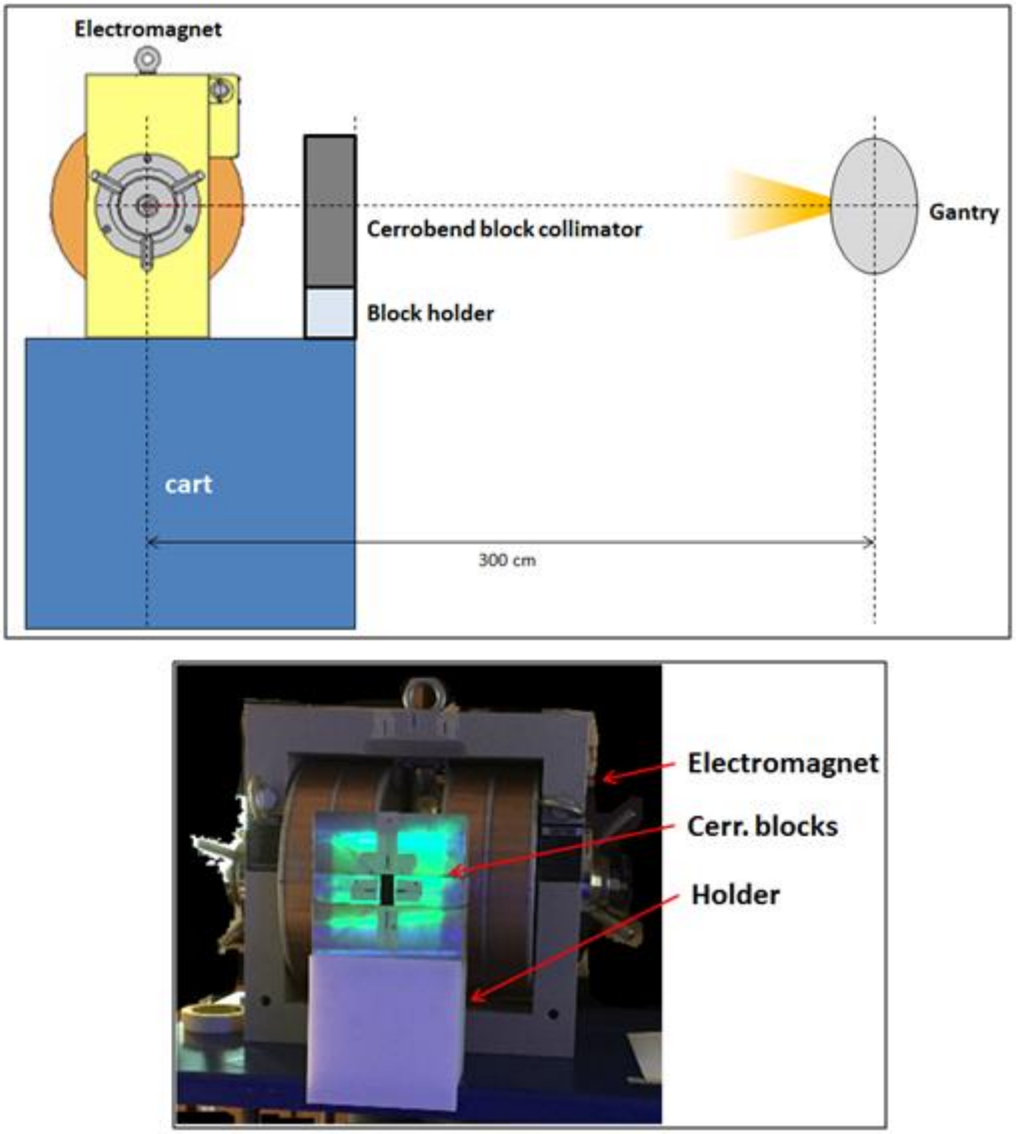

Figure 24: (Top) Schematic of the irradiation setup with the electromagnet at extended SAD setup. The center of the magnet is located 300 cm from the gantry. (Bottom) Photo of the experiment setup with the cerrobend blocks placed in front of the electromagnet to collimate the beam. The original field is shown by the green light field.

3.2.2. Magnetic field effects on Gafchromic® EBT3

Prior to EBT3 measurements, dose calibration was first performed to verify the dose response of the lot of EBT3 used throughout the thesis. The film was cut into 2 cm x 2 cm pieces and irradiated in the standard setup, using 100 cm SSD and solid water slabs that provided 10 cm build-up and 9 cm backscatter to the film piece. The irradiation was performed with no magnetic field.

For calibration, dose was plotted as a function of the change in the film's optical density before and after irradiation (netOD), and the data was fit to a 3rd order polynomial, as proposed by proposed by Devic *et al* and Sorriaux *et al* (39, 40). The dose delivered to the films was calculated following the TG-51 protocol using ion chamber measurements performed under the same conditions as used for the film irradiations. To measure the netOD, films were read out before irradiation (prescan) and at least 20 hours post-irradiation (postscan) in Epson Flatbed Scanner 1000XL, using Epson Scan (software). In order to keep the orientation and position of the film in the scanner consistent, a mask with cutouts that match the shape of the film pieces was attached to the scanner. Prescan values were subtracted from postscan values to account for any nonuniformity within the film piece and any OD change that might have occurred prior to the irradiation. The average difference between the prescan and the postscan of film pieces that had not been irradiated but were handled identical to the irradiated films represent how much OD has changed due to accidental exposures (e.g., exposure to room lighting). By subtracting the average netOD of unirradiated pieces as well, the true change in the OD due to the irradiation (netOD) was measured. All measurements were performed as triplicate.

After calibration, EBT3 was tested for magnetic field effect by comparing the EBT3 response curve for film pieces irradiated in magnetic field (B = 1.5 T) against the curve for pieces irradiated in zero magnetic field (B = 0). For this test, the films were prepared in 2 cm x 10 cm pieces to fit in the plexiglass phantom and were irradiated in the extended SAD setup with either the electromagnet on (B = 1.5 T) and off (B = 0) to 4 different dose levels. Because absolute dose measurement using an ion chamber was not feasible in the setup, four different monitor unit (MU) settings (1000, 4000, 7000, and 10000) were used, and instead of comparing absolute dose response curves, response to MU setting was compared between B = 0 and B = 1.5 T irradiations. The use of MU settings was justified because MU is a measure of the energy fluence, and under constant conditions and charged particle equilibrium, is proportional to dose. From calculations using the inverse-square law and the depth dose curve from the annual QA of the linear accelerator, it was estimated that about 0.001 Gy/MU would be delivered to the dosimeters, irradiating the dosimeters to approximately 1, 4, 7, and 10 Gy for the MU settings. All measurements were performed as triplicate.

The same read-out and netOD calculation process were followed as were done in the calibration process. Response curves were created by plotting relative dose (MU setting) as a function of netOD measured and by fitting to a 3rd order polynomial, as proposed by Devic *et al* and Sorriaux *et al* (39, 40). R-statistical software was used to perform analysis of variance (ANOVA) to test whether the presence of the magnetic field had a significant influence on the response curve.

3.2.3. Magnetic field effects on PRESAGE®

The effect of the magnetic field on PRESAGE® material was investigated, using regular cuvettes (1 cm x 1 cm x 4 cm) of PRESAGE® that fit into the plexiglass phantom. The cuvettes were delivered 1000, 4000, 7000, and 10000 MU in the extended SAD setup as well, either in B = 0 or B = 1.5 T. Due to the limited supply of PRESAGE® cuvettes at the time, duplicate measurements per dose level were made for B = 0 irradiations. Since the dose response of this formulation in B = 0 had already been confirmed in Section 2.3.1, duplicate measurements were considered sufficient. For B = 1.5 T irradiations, triplicate measurements were made per dose level. The netOD change due to irradiation was calculated the same way as in Section 2.2.2, by taking the difference between the average OD of the irradiated cuvettes and that of the unirradiated cuvettes that were handled identically. Since PRESAGE® is a relative dosimeter, dose response curves were plotted as netOD vs.

MU settings. ANOVA was performed in R-statistical software to test whether the magnetic field had a significant influence on the dose response curve.

3.3. Results

3.3.1. Calibration of Gafchromic® EBT3

Figure 25 shows the dose response of the Gafchromic® EBT3 film used throughout this thesis, showing the average netOD measured per dose level. Error bars were plotted as well but are not visible due to the small size. The calibration curve, which is dose as a function of netOD fit to a 3rd order polynomial, was

$$Dose\ [\mathrm{Gy}] = 30.349 * netOD^3 + 4.797 * netOD^2 + 10.018 * netOD$$

with an R^2 value of 0.999. Table 5 lists the data obtained from the calibration and noise-to-signal ratio (NSR) at each dose level, calculated as the percentage ratio of the sample standard deviation to the mean. The NSR was less than 1% for all dose levels except at 8.04 Gy, where one outlier was observed.

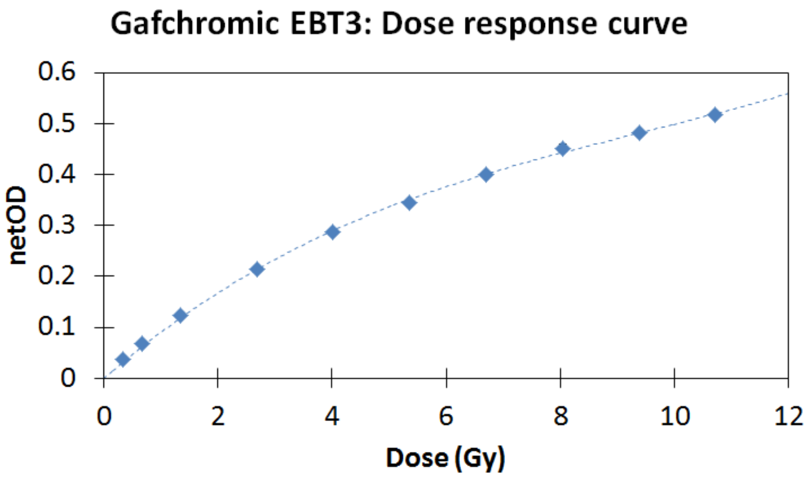

Figure 25: Calibration curve for Gafchromic® EBT3 film used for the project

Dose	netOD	mean netOD	Standard deviation	% NSR
0.335	0.036338	0.03623	0.000127	0.351213
0.335	0.03609			
0.335	0.036263			
0.67	0.06798	0.067621	0.000357	0.52837
0.67	0.067619			
0.67	0.067265			
1.34	0.124256	0.12386	0.000521	0.420475
1.34	0.124053			
1.34	0.12327			
2.68	0.214154	0.21394	0.000201	0.093985
2.68	0.213911			
2.68	0.213755			
4.02	0.288614	0.286595	0.00175	0.610646
4.02	0.285517			
4.02	0.285653			
5.36	0.344981	0.345484	0.001251	0.361979
5.36	0.344563			
5.36	0.346908			
6.7	0.399599	0.399657	0.000284	0.070966
6.7	0.399965			
6.7	0.399407			
8.04	0.444123	0.449715	0.009202	2.046248
8.04	0.444687			
8.04	0.460336			
9.38	0.482618	0.482156	0.000411	0.085297
9.38	0.481829			
9.38	0.482022			
10.72	0.516158	0.516444	0.000865	0.167578
10.72	0.515759			
10.72	0.517417			

Table 5: NetOD measured for each film pieces

3.3.2. Magnetic field effects on EBT3

Figure 26 shows the average response of EBT3 for the MU settings in B = 0 and B = 1.5 T. No visible difference was observed between the two response curves. The result from ANOVA in R-statistical software also showed no significant magnetic field effect, with a p-value of 0.6409. The code and input file for the analysis can be found in Appendix C (Figure 40, Table 11). Table 6 contains the netOD values obtained for each film that was used for the analysis. The last column in the table shows the average difference between the netOD from B = 0 and B = 1.5 T irradiations, displayed as the percentage of the average netOD at each dose level. The difference between B = 0 and B = 1.5 T film readings was less than 1.5 % for all dose levels.

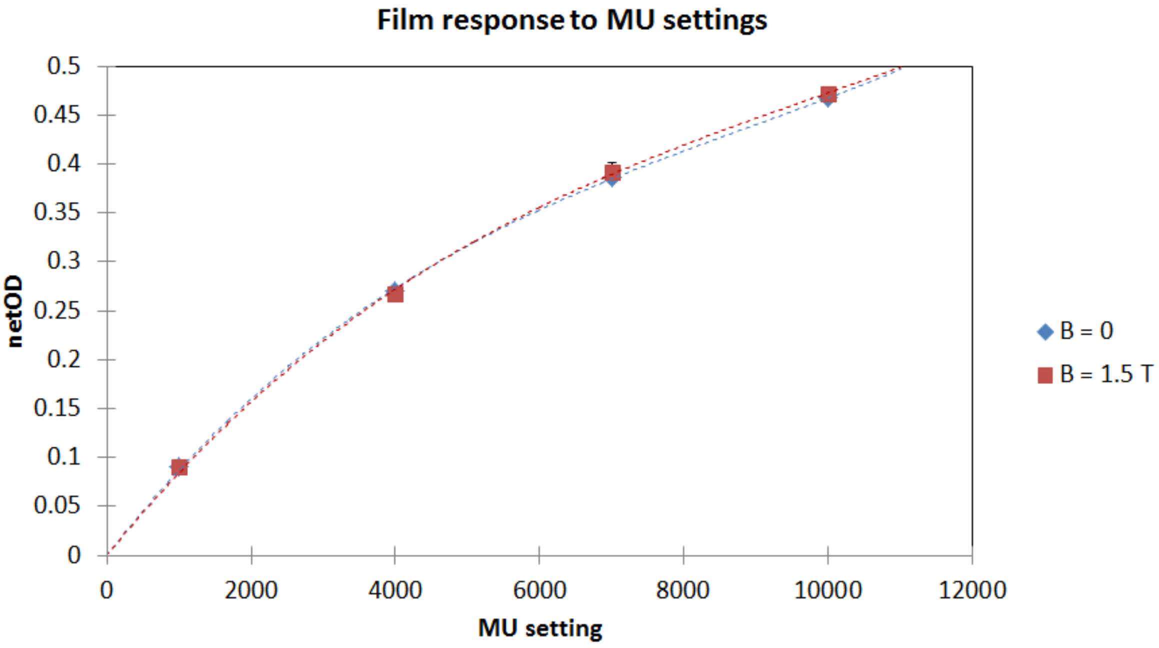

Figure 26: Relative dose response of films irradiated in B = 0 and B = 1.5 T.

B (T)	MU	netOD	$\Delta\left(\overline{(B = 0)} - \overline{(B = 1.5\ T)}\right)$ (%)
0	1000	0.090448	0.92063324
0	1000	0.089992	
0	1000	0.093232	
0	4000	0.270059	0.956389756
0	4000	0.269506	
0	4000	0.270282	
0	7000	0.386934	-1.42399686
0	7000	0.388017	
0	7000	0.385223	
0	10000	0.449999	-1.09110044
0	10000	0.47505	
0	10000	0.476249	
1.5	1000	0.089302	
1.5	1000	0.087467	
1.5	1000	0.094385	
1.5	4000	0.26788	
1.5	4000	0.26862	
1.5	4000	0.265601	
1.5	7000	0.401878	
1.5	7000	0.391622	
1.5	7000	0.383194	
1.5	10000	0.472235	
1.5	10000	0.470995	
1.5	10000	0.473358	

Table 6: NetOD values obtained for each film irradiated in B = 0 and B = 1.5 T.

3.3.3. Magnetic field effects on PRESAGE®

Figure 27 shows the relative dose response curves of PRESAGE® cuvettes, showing a decrease in the slope and implying an under-response in the presence of the magnetic field. The

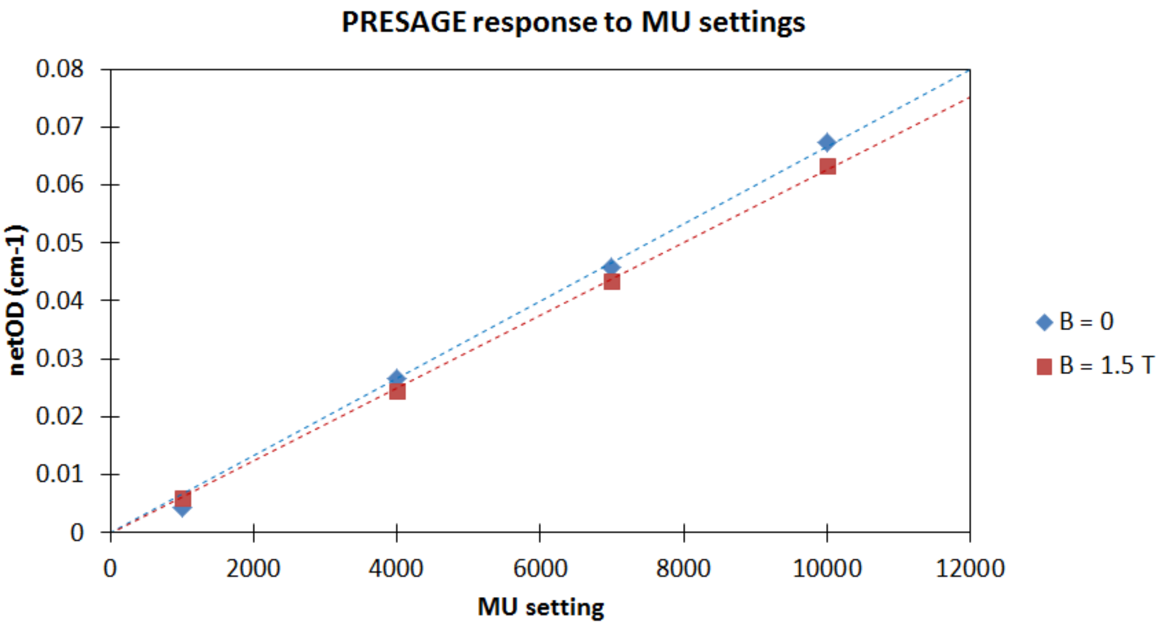

Figure 27: Relative dose response of PRESAGE® cuvettes irradiated in B = 0 and B = 1.5 T.

measured netOD for each cuvette is shown in Table 7. Despite the under-response, the response in B = 1.5 T was still strictly linear, with $R^2 > 0.99$. The result from the analysis on R-statistical software (Figure 41, Table 12) showed that the effect of the magnetic field on the sensitivity of PRESAGE® was statistically significant with p-value of $9.34*10^{-4}$. The 95% confidence interval of the change in the slope, due to the magnetic field, was ($-5.97*10^{-7}$/MU, $-1.83*10^{-7}$/MU), for the original slope that was calculated to be $6.662*10^{-6}$ (MU^{-1}). Thus the maximum change in the sensitivity due to the magnetic field, in 95 % confidence level, was $\frac{-5.97*10^{-7}}{6.662*10^{-6}} = -0.089$, corresponding to a 9 % under-response.

B(T)	MU	netOD
0	1000	0.0035
0	1000	0.005
0	4000	0.0253
0	4000	0.0281
0	7000	0.045
0	7000	0.0468
0	10000	0.0657
0	10000	0.069
1.5	1000	0.0062
1.5	1000	0.0049
1.5	1000	0.0069
1.5	4000	0.0259
1.5	4000	0.0237
1.5	4000	0.0239
1.5	7000	0.0431
1.5	7000	0.0432
1.5	7000	0.0439
1.5	10000	0.0628
1.5	10000	0.0635
1.5	10000	0.0637

Table 7: NetOD values obtained for each PRESAGE® cuvette irradiated in B = 0 and B = 1.5 T.

3.4. Discussion

The ANOVA result from R-statistical software showed that film response was unaffected by the magnetic field. The difference in netOD values in B = 0 and B = 1.5 T cases, as shown in Table 6, was less than 2 %, and considering the uncertainties involved in the experiment setup and the beam output, the difference was not significant. This established the Gafchromic® EBT3 film as a standard for evaluating the performance of PRESAGE® dosimetry in magnetic field in SA 3.

On the other hand, PRESAGE® showed under-response in the presence of the magnetic field. On a 95 % confidence level, it was expected that the maximum decrease in the sensitivity due to the magnetic field would be within 9 %. However, since PRESAGE® dosimeters are relative dosimeters and the response remained strictly linear with dose, the change in the PRESAGE® response in the magnetic field can be accounted for by applying a small correction factor for the sensitivity. For the scope of this thesis, where the aim was to compare film and PRESAGE® response in the identical setting with B = 1.5 T magnetic field, this posed no problem since the magnetic field supplied by the electromagnet stayed constant.

Chapter 4—Specific Aim 3

4.1. Rationale

In Chapter 3, EBT3 was established as the standard for the performance evaluation of PRESAGE® dosimetry in magnetic field. In this chapter, the ability of PRESAGE® dosimetry to accurately measure the dose distribution in the magnetic field was assessed by comparing PRESAGE® measurements to EBT3 measurements. In Chapter 3, the response of the PRESAGE® material was shown to be affected by the magnetic field but still strictly linear to dose, so relative dosimetry using the PRESAGE® system was still expected to be reliable.

In the first section of this chapter, the baseline for film-PRESAGE® comparison was established by comparing the measurement by the two systems in the absence of the magnetic field. In the second section of this chapter, the hypothesis of this thesis was tested: "the dose distribution delivered in the presence of a magnetic field can be measured with PRESAGE® dosimeters to 5 %/3 mm agreement with that measured by film." The region of comparison included the region affected by the ERE, since the ability to capture the volumetric ERE is a big part of the reason that 3D dosimetry is expected to be beneficial for the quality assurance of MRgRT.

4.2. Methods

4.2.1. Validating workflow: baseline for film-PRESAGE® comparison

4.2.1.1. Irradiation setup

A short cylindrical PRESAGE® dosimeter was produced to fit into an ABS plastic phantom designed for the experiment. The phantom was 3D printed to provide adequate buildup and scatter around the dosimeter. The PRESAGE® dosimeter was designed to contain a coaxial cylindrical cavity to demonstrate the goodness of measurement around a cavity in the absence of the magnetic field.

Two additional short cylindrical PRESAGE® dosimeters were produced as "dummies," such that the sum of their heights was equal to the height of the experiment PRESAGE® dosimeter. An EBT3 film piece, whose response was validated in Section 3, was cut and sandwiched in between the dummies (Figure 28). This ensured that upon a successful spatial registration, the film dose would match a cross-sectional plane in the dose distribution measured by the PRESAGE® dosimeter.

The dosimeters were irradiated to contain three different dose regions. With the gantry at 90˚, the phantom containing the dosimeter was placed at 100 cm SSD and was irradiated using a 10 cm x 10 cm field with the collimators tilted to 45˚. The collimator was positioned at an angle to test the goodness of spatial registration in the top-bottom dimension of the dosimeter. After delivering 530 MU, the position of the phantom was shifted to deliver another 530 MU, creating a high-dose region (Figure 29, Figure 30). This allowed the dose ranging from 0 to 10 Gy to be delivered to the dosimeters. For both the film and the PRESAGE® dosimeter, prescan was done just before the irradiation. The postscans for the film and the PRESAGE® dosimeter were done 24 hours and 2 hours post-irradiation, respectively.

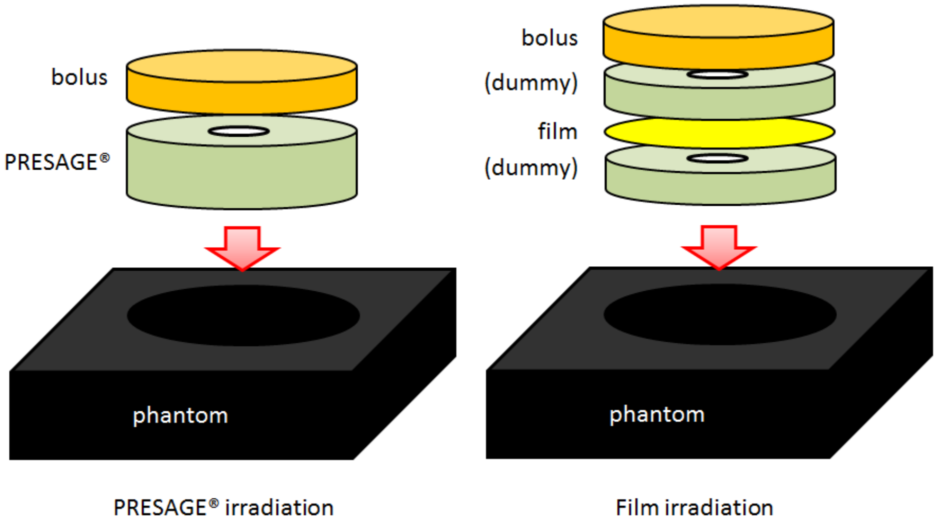

Figure 28: ABS plastic phantom and (left) setup for PRESAGE® dosimeter irradiation and (right) setup for film irradiation.

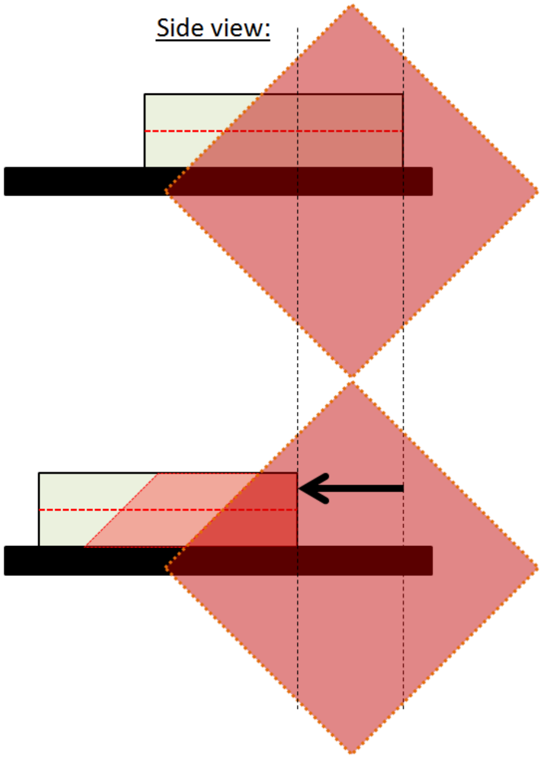

Figure 29: Side image of the setup for the experiment, shown without the phantom. The phantom is placed such that the dosimeter lies flat on the couch, with gantry at 90˚. The red diamond shows the position of the radiation field, which remains consistent, while the dosimeter is shifted for the second irradiation, creating different dose regions in the dosimeter.

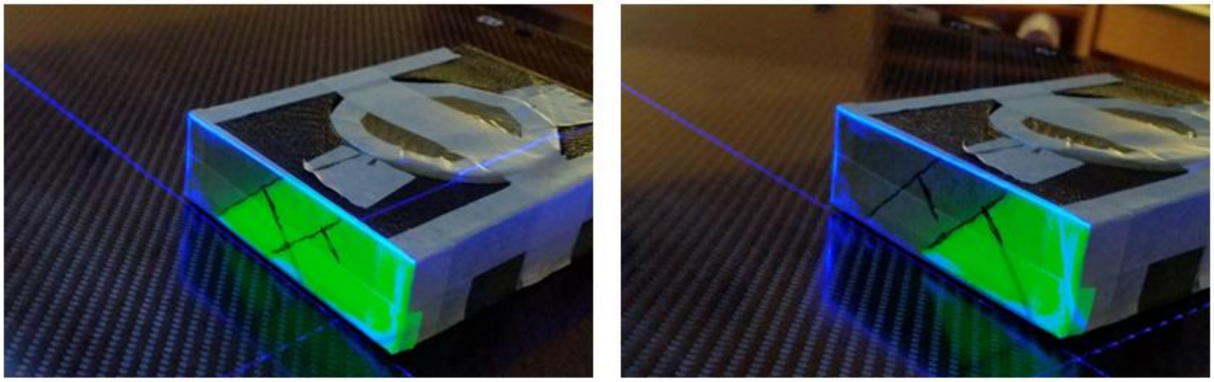

Figure 30: The phantom containing the dosimeter on the treatment couch, positioned based on laser marks. After the first irradiation in one position (left), the phantom is shifted to create a high dose region (right). Pen markings are made on the masking tapes on the top surface of the phantom to note the position of the registration marks.

4.2.1.2. Image registration

After film and PRESAGE® dosimeters were read out using the flatbed scanner and the optical-CT, respectively, the images were spatially registered for gamma analysis. The rotational orientation was marked using three fiducial markers on the PRESAGE® dosimeter and the matching pen markings on the film. The ABS plastic phantom was also marked to match the irradiation orientation of the film and PRESAGE® dosimeters (Figure 30). The fiducial markers on the PRESAGE® dosimeter were attached only during the prescan and were detached for the irradiation. Removing the fiducials allowed the dosimeter to fit into the phantom and prevented the fiducials from being subtracted during the image processing chain of the optical-CT. The position of the fiducial markers was determined such that the streaking artifact, caused by the intense attenuation of light rays in the optical-CT due to the fiducials, would not affect the plane of analysis. After the film and PRESAGE® images were imported into the dose comparison software, they were spatially registered by using fiducial registration module and image transformation module.

4.2.1.3. Dose comparison

The Epson flatbed scanner and the optical-CT used to read out film and PRESAGE® dosimeters yielded different file types. Among the programs used for analysis of medical images, 3D Slicer was used for this project for the ease of image registration and compatibility with different image formats involved in this project. 3D Slicer is a multi-platform, open source software package developed for the visualization and computation involving medical images. The gamma analysis in 3D Slicer had been validated (41) and also was independently tested to be accurate (Appendix B). It was already proven in a number of studies that PRESAGE® and film measurements have a high agreement (14, 16, 35, 42), but the workflow specific to this project was yet to be validated. Thus this section also served the purpose of validating the use of 3D Slicer for image registration and gamma analysis to compare film and PRESAGE® measurements.

For dose comparison using 3D Slicer, the following steps were taken. The initial data read-out from film and PRESAGE® dosimeters was in the form of netOD, which needed to be converted into dose (Gy). Film netOD was averaged among three independent measurements and converted to dose by using the calibration curve obtained in Section 3.3.1. PRESAGE® reading was scaled to the dose distribution calculated from the film, since it was proven that PRESAGE® response was strictly linear to dose even in the magnetic field. For scaling, an ROI was defined in the high-dose region with a high SNR, and the multiplication factor that was needed to match the PRESAGE® reading to the film dose was calculated. The ROI was defined prior to spatial registration due to the limits in the workflow, but it was placed as consistently as possible, based on the fiducial markers and film markings.

After spatial registration, the gamma analysis was performed using the dose comparison module in 3D Slicer. The areas containing film markings in the film and edge artifact in PRESAGE® were excluded from the analysis to achieve the best-case scenario. The gamma analysis gave the maximum agreement possible between film and PRESAGE® in the workflow for this thesis and set the baseline for EBT3-PRESAGE® comparison. Both global and local gamma analyses were performed at tighter gamma criteria of 3 %/3 mm, with no dose threshold. The total workflow up to dose comparison is summarized in Figure 31.

4.2.2. Measurement of the ERE using film and PRESAGE® dosimeters

The hypothesis of this project was that the dose distribution delivered in the presence of a magnetic field can be measured with a PRESAGE® dosimeter to a 5 %/3 mm agreement with that measured by film. As in Chapter 3, the magnetic field was provided by the electromagnet, which provided a 1.5 T magnetic field in the center of the pole caps. To suspend the dosimeters in the region of the magnetic field in the electromagnet, a second ABS phantom was 3D printed. The second piece

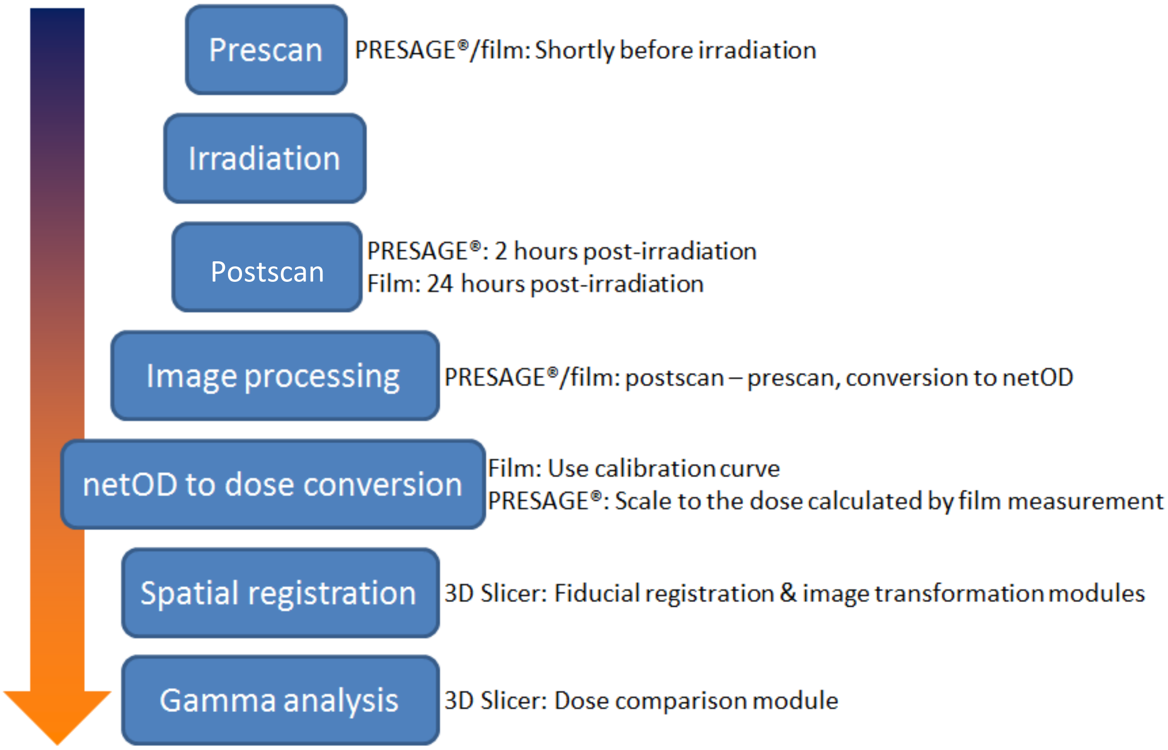

Figure 31: Workflow for film-PRESAGE® comparison

was designed as a holder for the first ABS plastic piece used in Section 4.2.1, which served as the insert. The insert piece containing the dosimeter could be slid in and out to switch out the dosimeterswhile the holder remained fixed between the pole pieces (Figure 32). Like the plexiglass phantom used in Chapter 3, this ABS plastic phantom ensured high setup reproducibility.

In order to demonstrate the ability of the PRESAGE® system to measure the ERE, the PRESAGE® dosimeter was designed with a coaxial cylindrical cavity as in Section 4.2.1. Due to the limited supply of the dosimeters, the experiment was performed with two PRESAGE® dosimeters that

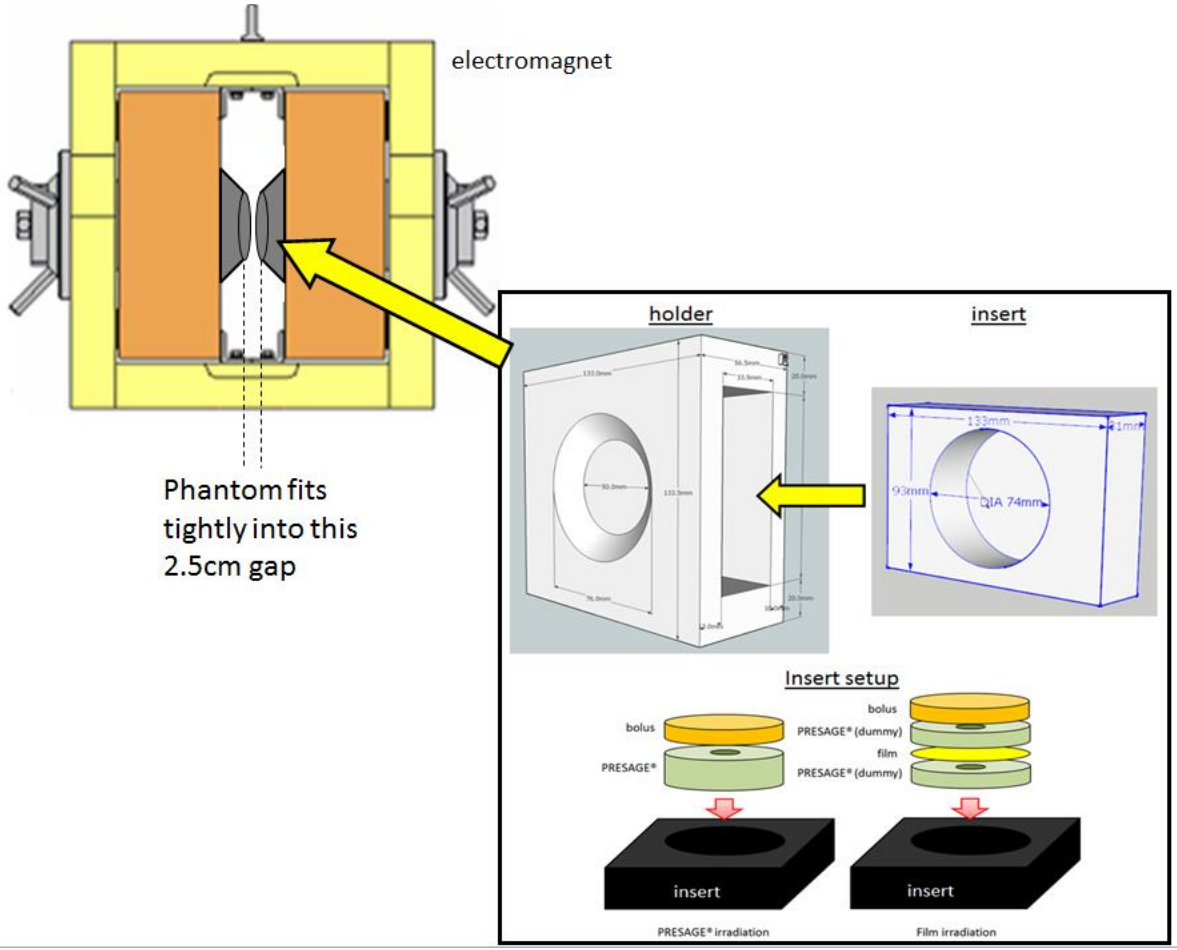

Figure 32: A schematic showing the design and setup of the ABS plastic phantom parts (holder and insert) containing the dsoimeters.

were conserved in the freezer for about 1 month. Film measurements were repeated three times for better statistics. The workflow was the same as in Section 4.2.1, as shown in Figure 31. The ROI used for scaling PRESAGE® to film was defined in in area of moderately high dose, 2.5 ~ 3 cm into the dosimeter, to reduce the uncertainty due to signal fluctuation in the dosimeter.

For dose comparison, local gamma analysis was performed to compare the average film dose to the dose distribution measured by PRESAGE® dosimeter 1 and 2, separately. Local gamma analysis was used because in comparing film and PRESAGE® dosimetry system, ideally PRESAGE® should agree with film in all dose regions. By using local gamma, the performance of the PRESAGE® system in the low dose region was tested as rigorously as in the high dose region. The gamma analysis was performed with and without $D > 1\ Gy$ dose constraint.

4.3. Results

4.3.1. Validating workflow: baseline for film-PRESAGE® comparison

Figure 33 shows the registered film-PRESAGE® images and the segment structure that was created for the gamma analysis, excluding pen markings on the film and the edge artifact in PRESAGE® image. The segment structure had a margin around the edge artifact to achieve the best-case scenario. The resulting gamma map is shown in Figure 34. The passing rate for global and local gamma analyses were 99.61 % and 96.70 %, respectively.

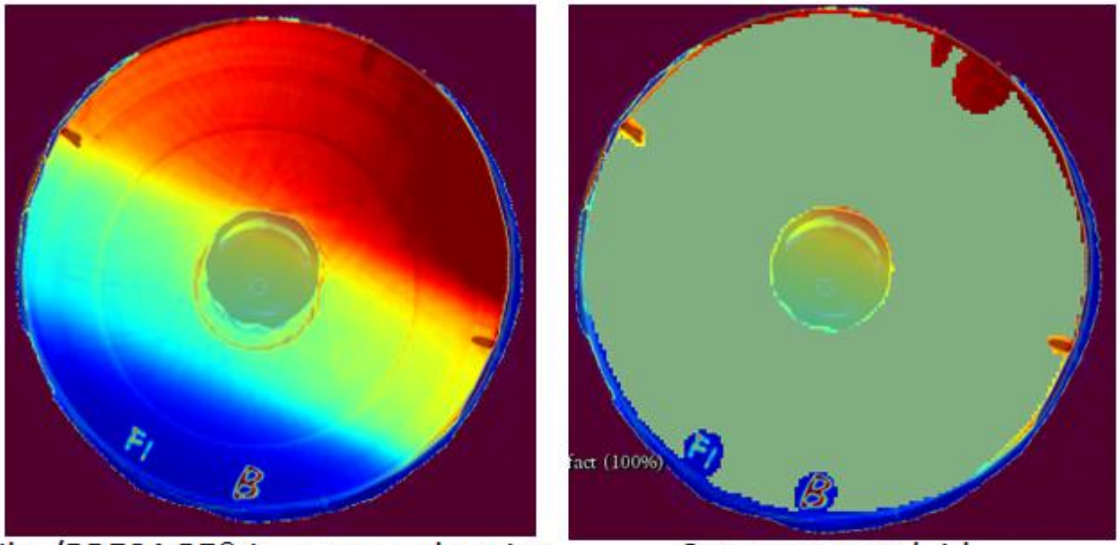

Film/PRESAGE® image overlapping

Segment overlaid

Figure 33: (Left) Film and PRESAGE® images spatially registered and (right) the segment structure overlaid. Gamma analysis in 3D Slicer is performed only within the mask structure.

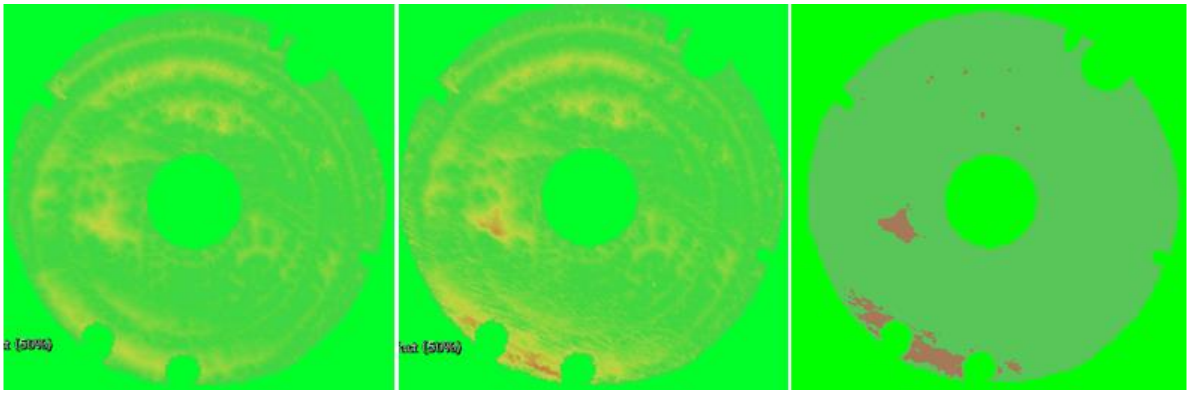

Figure 34: Gamma map produced from global (left) and local (mid) gamma analysis. The gamma map on the right is a binary representation of the local gamma map, showing the failing points in red.

4.3.2. Measurement of the ERE using film and PRESAGE® dosimeters

Figure 35 shows the average film dose measurement overlaid on top of the dose distributions measured by the two PRESAGE® dosimeters, the segment structure defined for the gamma analysis, and the local gamma maps calculated with no dose constraint. The pictures are shown such that the beam is entering the dosimeter from the top of the pictures. The segment structure was defined tightly around the region of the edge artifact. Estimating from the physical size of the cavity measured by a caliper, the region excluded from the analysis due to the edge artifact was less than 2 mm. However, the finite edge artifact resulted in streaking around the cavity, which affected the image quality inside the dosimeter body. Although not shown in the figure, local gamma maps were also calculated with a dose constraint of $D > 1\ Gy$, which only excluded the points outside the beam from the analysis. The passing rates calculated for the local gamma analyses, with and without the dose constraint, are shown in Table 8. The gamma pass rates for PRESAGE® dosimeter 1 was 92.00 % for both analyses

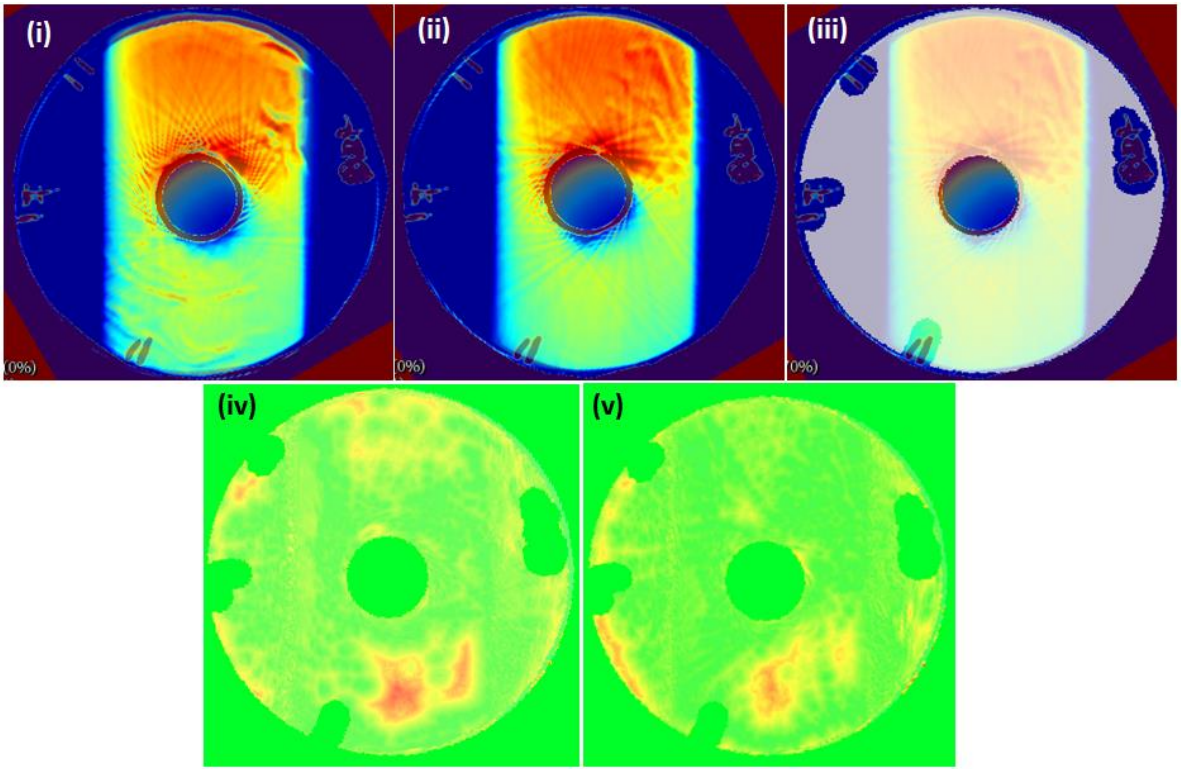

Figure 35: (i) Dose from the averaged film and PRESAGE® dosimeter 1 overlaid, (ii) dose from the averaged film and PRESAGE® dosimeter 2 overlaid, (iii) segment structure for gamma analysis overlaid, (iv) gamma map for averaged film vs. PRESAGE® dosimeter 1, (2) gamma map for averaged film vs. PRESAGE® dosimeter 2

	PRESAGE® dosimeter 1	PRESAGE® dosimeter 2
Averaged film (no dose constraint)	92.00 %	95.56 %
Averaged film (dose constraint)	92.00 %	94.17 %

Table 8: Local gamma analysis passing rates calculated with 5 %/ 3 mm gamma criteria, for averaged film vs. PRESAGE® dosimeter 1 and 2, with and without dose constraint of (D > 1 Gy).

performed with and without the dose constraint. The pass rates for PRESAGE® dosimeter 2 were even higher, with 95.56 % with no dose constraint and 94.17 % with constraint.

Figure 36 shows the line profiles taken through the region of edge artifact, across the cavity, obtained along the same axis for EBT3 and both PRESAGE® dosimeters. The line profiles agree well with one another qualitatively, and it can be observed that PRESAGE® dosimeters have captured the dose enhancement and build-up due to the ERE. On the other hand, a significantly high level of noise can be seen in both PRESAGE® dosimeters.

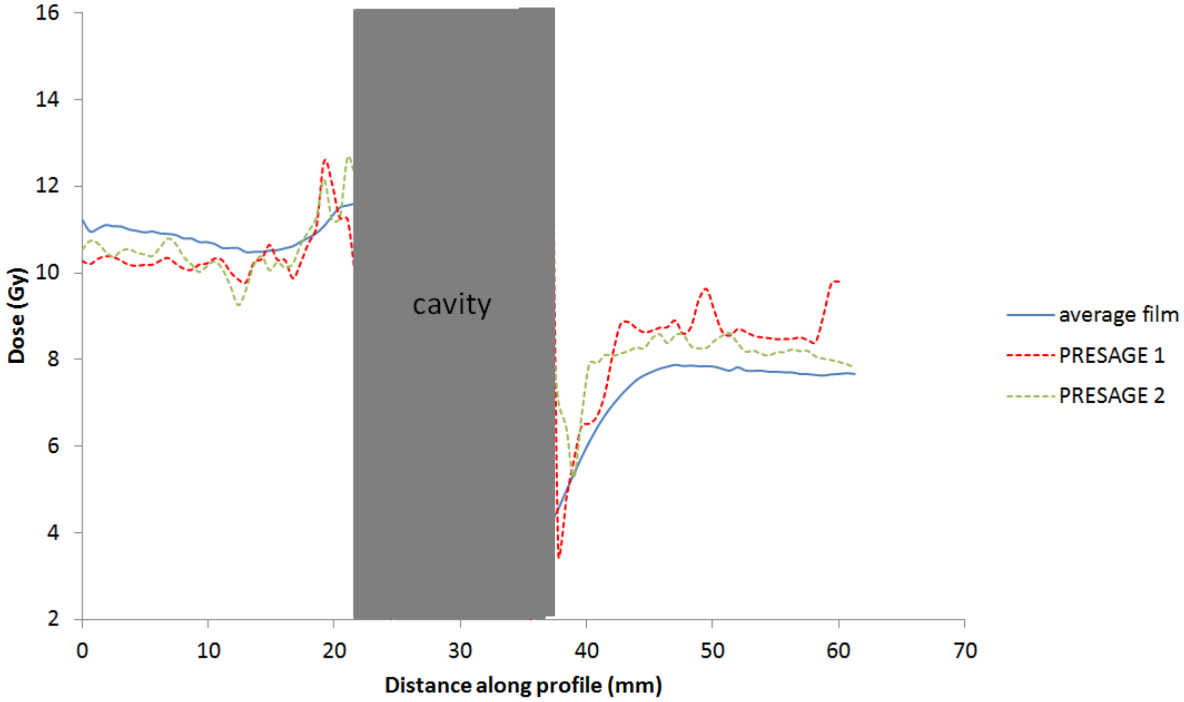

Figure 36: Line profiles of averaged film, PRESAGE® dosimeters 1, and PRESAGE® dosimeter 2, taken along the same axis.

4.4. Discussion

4.4.1. Validating workflow: baseline for film-PRESAGE® comparison

This experiment used a simple irradiation scheme involving three dose regions—low, medium, high—to show that the workflow using 3D Slicer is feasible in various dose regions. In order to set the best-case scenario as the baseline for comparison, the region of severe edge artifact was excluded from analysis. Both global and local gamma tests showed high passing rates above 96%, as expected from the results shown in the references (14, 16, 35, 42). The passing rate for local gamma analysis was lower than global gamma because for local gamma, the dose difference for the voxels in the low dose region is tighter than in global gamma calculation. The local gamma test failed more towards the extreme low dose region, in the unirradiated region of the dosimeter. This region was shown to have received nearly 0 Gy, which made the dose difference criteria too tight to be achieved, and thus did not pose a concern.

One noticeable point in the gamma maps is the presence of yellow concentric rings, where the yellow represented gamma indices close to 1 and close to failing. These ring artifacts were also present in the reconstructed image (Figure 33) and were proven to be the result of a bad flood field used in the reconstruction. In other scans, where the flood field was obtained more carefully, the ring artifact was not present.

4.4.2. Measurement of the ERE using film and PRESAGE® dosimeters

Both PRESAGE® measurements agreed well with the averaged film measurement. The passing rates were slightly lower than in the best-case scenario of no magnetic field and no ERE (as shown in Section 4.3.1), but they were still higher than the 85 % threshold that IROC-Houston uses in the credentialing process or the 90 % threshold used for IMRT QA, implying a good agreement between the dose distributions measured by film and PRESAGE® dosimeters. The PRESAGE® images contained some artifacts: the streaking around the cavity was due to the finite edge artifact at the cavity surface, and wavy patterns in the dosimeter were due to schlieren banding, which refers to regions of slightly different optical properties created during the dosimeter manufacturing process. Some measures can be taken in the future to reduce these artifacts. A reconstruction algorithm based on iterative reconstruction is under development (29, 30) and is expected to reduce the streaking due to the edge artifact. The wavy artifact due to schlieren banding can be reduced with more care and skill in the manufacturing process. From the gamma maps and calculated passing rates, however, neither the presence of streaking nor the schlieren banding seems to have a significant effect on the agreement between PRESAGE® and film.

The gamma maps in Figure 35 show that most points that fail the gamma criteria are towards the bottom of the image—in the deeper side of the dosimeter where the dose delivered is lower. This may be due to the inhomogeneous magnetic field in the electromagnet. In Chapter 3, PRESAGE® response was shown to be affected by the magnetic field. If the change in the sensitivity of PRESAGE® is correlated with the strength of the magnetic field, the sensitivity inside the dosimeter would also vary slightly, depending on the local strength of the magnetic field. Earlier, the profile of the magnetic field in the electromagnet was shown to be relatively uniform in the central 3 ~ 4 cm region in the electromagnet (Figure 23), with the strength dropping along a steep slope farther away. Since the ROI defined for scaling PRESAGE® to film was defined in the shallow region receiving a higher dose than in further depth, the inhomogeneity in the magnetic field may explain the sudden appearance of failing points on the deeper side of the dosimeter. Studying the dependence of PRESAGE® sensitivity on the strength of the magnetic field will be able to clarify if the failing points in the low dose region are indeed due to the magnetic field effects. Nevertheless, the high passing rates show that this effect is minimal in the context of practical applications, and that PRESAGE® is able to perform as well as film even in some magnetic field inhomogeneity.

In the line profiles, the noise in the PRESAGE® is due to the streaking arising from the finite amount of edge artifact at the cavity surface. Even in the presence of the noise, the line profiles for both PRESAGE® dosimeters clearly show the dose enhancement and build-up due to the ERE, demonstrating the ability of PRESAGE® dosimeters to make measurements that agree well with the film measurements, in the region affected by the ERE.

Chapter 5 – Conclusion

The purpose of this thesis was to demonstrate the validity of PRESAGE® dosimetry in magnetic field by showing that PRESAGE® can accurately measure the ERE, a phenomenon specific to and important in MRgRT. This goal was achieved in three steps. In SA 1, different RI-matching methods were tested to reduce the edge artifact, in order to capture the ERE using PRESAGE® dosimeters. A statistical time-series method was proposed and utilized to compare the different methods, which revealed that the conventional method of using the matching fluid performed the best in suppressing the edge aritfact. In SA 2, Gafchromic® EBT3 film was established as the standard for evaluating PRESAGE® performance by showing that the response of EBT3 was not affected by the magnetic field. The in-house made PRESAGE® formulation that was used throughout this thesis was also tested for magnetic field effects, which showed ~ 9 % under-response in a 1.5 T magnetic field. The response, however, remained strictly linear, and it was concluded that the magnetic field effect would not interfere with using PRESAGE® as relative dosimeter in this thesis. In SA 3, EBT3 and PRESAGE® were compared in measuring the dose distribution in a relatively simple scenario, with no magnetic field, and finally, in measuring the ERE in the magnetic field. The first set of measurements provided the baseline for comparing film and PRESAGE® for the workflow used for this thesis. In the latter set of measurements, where the dose distribution modified by the ERE provided a more challenging case, the agreement between film and PRESAGE® was only slightly degraded, with passing rates still well over 90 %. Thus hypothesis of this thesis—“ the dose distribution delivered in the presence of a magnetic field can be measured with a PRESAGE® dosimeter to 5 %/3 mm agreement with that measured by film”—was accepted.

The result of this thesis shows that PRESAGE® dosimetry is as reliable as Gafchromic® EBT3 film dosimetry in the magnetic field. There are several points to be noted for future work. First, in SA 1, projection images that were taken seven days after filling-in the cavity showed a great potential for the fill-in method. As suggested in Section 2.3.2, the fill-in method will be able to reach the full potential if an optical-CT system that does not require a prescan is developed. Second, SA 2 showed that PRESAGE® was prone to magnetic field effect. Although it did not affect the measurement outcome in the macroscopic level, in order to use PRESAGE® for a variety of applications, a more comprehensive study on the dependence of PRESAGE® sensitivity on the strength of the magnetic field will need to be conducted. Furthermore, investigations into the microscopic process that leads to the under-response will be beneficial for developing the PRESAGE® formulation that exhibits less or no magnetic field effect.

Appendix A. Change-point detection method

The change-point detection method considers a time-series of n observations: $\mathbf{y} = \{y_1, \dots, y_n\}$ and assumes that the data can be broken into $m+1$ stationary segments. For $j = 1, \dots, m+1$, the jth stationary segment is modeled by a stationary process $\mathbf{x_j} = \{x_t^{(j)}\}$, $t \in Z$, such that

$$x_{t-\tau_{j-1}}^{(j)} = y_t, \qquad \tau_{j-1} \le t \le \tau_j$$

This is illustrated in Figure 37.

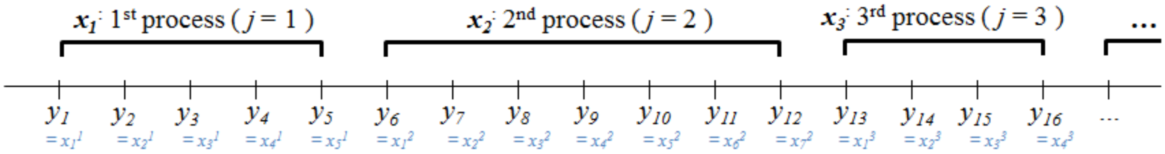

Figure 37: Illustration of n observations (y) broken into segments (x).

Due to the nature of the dose delivery process, the dose at one point is expected to be correlated with the dose at an adjacent point. In order to capture this dependence, this model assumes that each segment in a line profile follows a first-order autoregressive (AR(1)) model, where for an observation y_t in one segment in the line profile,

$$y_t = \mu + \varphi y_{t-1} + \epsilon_t,$$

where $\epsilon_t \sim$ iid $N(0, \sigma^2)$.

The change-point detection problem is solved by adopting the minimum description length (MDL) principle as the criterion function. The MDL principle is a formalization in which the best hypothesis for a dataset is the one that best compresses the data by best capturing the regularity in the data. Accordingly, the code works by minimizing the MDL criterion function

$$\mathrm{MDL}(m, \Lambda, \Psi) = \log m + (m+1)\log n + \sum_{j=1}^{m+1} \frac{3}{2}\log n_j - \sum_{j=1}^{m+1} L(\theta_j; \mathrm{x_j})$$

where $\Lambda = (\tau_1, \ldots, \tau_m)$, $\Psi = (\theta_1, \ldots, \theta_{m+1})$, m is the number of change-points, n is the sample size of the whole dataset, n_j is the length of the jth segment, and $L(\theta_j; \mathrm{x_j})$ is the likelihood for the jth segment. Given the location of the break-points, it is assumed that the jth segment is completely specified by a parameter vector θ_j, where $\theta_j \in \Theta \subset \mathrm{R^d}$, where $d \in \mathrm{N}$, is a compact parameter space.

Due to the nature of dose delivery, dosimeter response, and the read-out process, one may expect a certain degree of natural fluctuation, gradient, or trend in the line profile that is not related to the edge artifact. To ensure that the code does not break the dataset into an infinite number of segments based on the insignificant fluctuations, it is assumed that there exists an $\epsilon_\tau > 0$ such that $\min_{1\le j\le m+1}\left|\tau_j - \tau_{j-1}\right| > \epsilon_\tau$. This condition can also be imposed by requiring $\Lambda \in A_{\epsilon_\lambda}^m$, where

$$A_{\epsilon_\tau}^m = \{\tau \in (0,n)^m : 0 < \tau_1 < \cdots < \tau_m, \qquad \tau_i - \tau_{i-1} \ge \epsilon_\tau, \qquad i = 1, \ldots, m\}$$

Under this constraint, the number of change-points is bound by $M = \left[\frac{n}{\epsilon_\tau}\right] + 1$. Thus the change-point detection problem estimates the number of change-points, their locations, and the parameters in each of the segments by solving

$$\left(\hat{m}, \hat{\Lambda}, \hat{\Psi}\right) = \arg \min_{m \le M, \Psi \in \Theta^{m+1},} \mathrm{MDL}(m, \Lambda, \Psi)$$

where $\hat{\Lambda} = (\hat{\tau}_1, \ldots, \hat{\tau}_m)$, $\hat{\Psi} = (\hat{\theta}_1, \ldots, \hat{\theta}_{m+1})$. The parameters $\hat{\theta}_1, \ldots, \hat{\theta}_{m+1}$ are estimated such that

$$\hat{\theta}_j = \arg\max_{\theta \in \Theta} L(\theta; \hat{\mathrm{x}}_j)$$

where $\hat{x}_j = \{\, y_t : \left[\hat{\tau}_{j-1}\right] + 1 < \; t \le [\hat{\tau}_j] \,\}$ is the jth segment under the estimation.

Appendix B. Testing for the validity of the gamma analysis on 3D Slicer

3D Slicer is a free and open source software package for analysis and visualization of medical images. It has a dose comparison module that allows 3D gamma analysis, which allows comparing volumetric dose distributions. The validity this analysis had been shown, but the software went through some minor modifications to be used for this project (41). This appendix shows a validation of the gamma analysis algorithm after the modifications were made, which was performed by cross-comparing the gamma result of 3D Slicer with that of another independent Matlab code. The Matlab code was implemented and modified from the gamma code that was used in Scherman (2009), where the original code was validated (43).

Two datasets were generated in Matlab, each containing one 100 x 100 reference matrix and one 100 x 100 target matrix, both consisting of random numbers between 0 and 10 (Figure 38). The matrices contain a square area with fixed values of 0 and 1, where the gamma index is bound to be bigger than 1. The matrices were converted into nii format to be imported into Slicer to use its dose comparison module. For both datasets, global and local gamma analyses were performed with 3% / 3 mm gamma criteria with no dose threshold. The calculated pass rates perfectly agreed between the Matlab code and 3D Slicer, for both dataset and gamma method (
Table 9) and proved the validity of the gamma analysis tool in 3D Slicer.

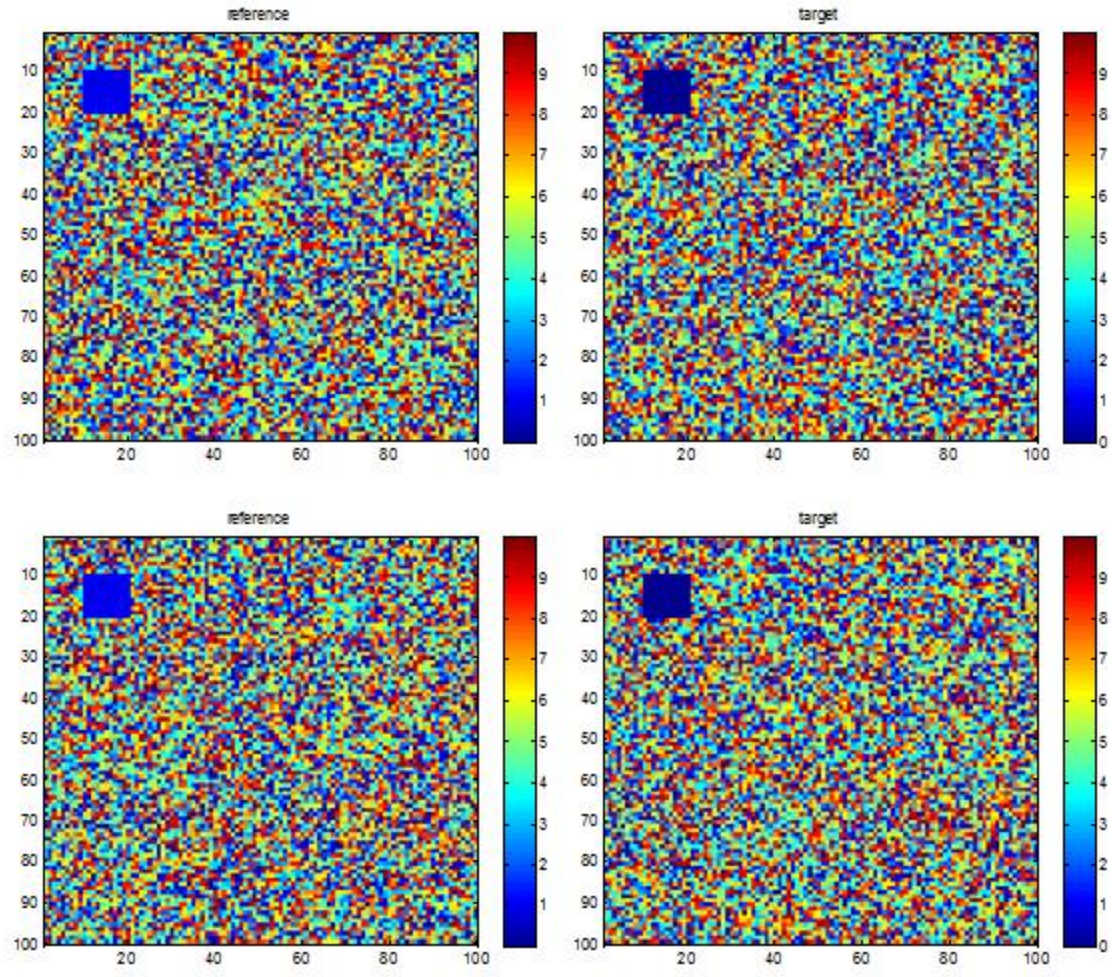

Figure 38: The reference and target matrix generated in Matlab. The square areas in the upper left corner of the matrices were given fixed values of 0 and 1.

	Dataset 1		Dataset 2	
	Matlab	Slicer	Matlab	Sicer
Global gamma	86.62%	86.62%	87.44%	87.44%
Local gamma	36.72%	36.72%	37.81%	37.81%

Table 9: Results of gamma analysis for dataset 1 and 2.

Appendix C. Codes and data

```
> x <- read.table("2016-11-12cuvettereadings.csv",header=T,sep = ",")
> dose <- x$Dose
> netOD <- x$netOD
> batch <- x$Batch

> ### Presage cuvette linear fit
> fit.1 <- lm(netOD ~ -1 + dose)
> fit.2 <- lm(netOD ~ -1 + dose + batch:dose)

> summary(fit.2)

Call:
lm(formula = netOD ~ -1 + dose + batch:dose)

Residuals:
       Min         1Q     Median         3Q        Max 
-0.0035391 -0.0014790 -0.0005897  0.0003672  0.0028641 

Coefficients:
           Estimate Std. Error t value Pr(>|t|)    
dose       9.048e-03  8.473e-05 106.789   <2e-16 ***
dose:batch 1.095e-04  1.198e-04   0.914    0.375    
---
Signif. codes:  0 ‘***’ 0.001 ‘**’ 0.01 ‘*’ 0.05 ‘.’ 0.1 ‘ ’ 1

Residual standard error: 0.001793 on 15 degrees of freedom
Multiple R-squared:  0.9994,	Adjusted R-squared:  0.9993 
F-statistic: 1.155e+04 on 2 and 15 DF,  p-value: < 2.2e-16
```

Figure 39: R code used to evaluate the effect of batch difference on the calibration curve. P-value is shown in red. With p >> 0.05, there is no interbatch variability observed.

B1dose	B1	B2dose	B2
1	0.008	0.5	0.0031
3	0.0258	1	0.0069
5	0.0452	3	0.026
7	0.0598	5	0.0452
9	0.0794	7	0.0623
9	0.0835	9	0.0823
9	0.0843	9	0.0824
11	0.0999	9	0.0837
		11	0.1019

Table 10: Input for the R-code shown in Figure 39, used to test for inter-batch variability in PRESAGE®

```
> x <- read.table("Beffect-film input.csv",header=T,sep = ",")
> MU <- x$MU
> netOD <- x$netOD
> MF <- x$MF

> ### films 3rd order polynomial fit
> fit.1 <- lm(MU ~ -1 + netOD + netOD:MF + I(netOD^2) + I(netOD^2):MF + I(netOD^3)
+ I(netOD^3):MF)
> fit.2 <- lm(MU ~ -1 + netOD + I(netOD^2) + I(netOD^3))
> anova(fit.1,fit.2)

Analysis of Variance Table

Model 1: MU ~ -1 + netOD + netOD:MF + I(netOD^2) + I(netOD^2):MF + I(netOD^3) +
    I(netOD^3):MF
Model 2: MU ~ -1 + netOD + I(netOD^2) + I(netOD^3)
  Res.Df     RSS Df Sum of Sq      F Pr(>F)
1     18  974066
2     21 1066873 -3    -92808 0.5717 0.6409
```

Figure 40: R-code used for the ANOVA analysis between film response in B = 0 and B = 1.5 T. The p-value is shown in red.

MF	MU	netOD
0	1000	0.090448
0	1000	0.089992
0	1000	0.093232
0	4000	0.270059
0	4000	0.269506
0	4000	0.270282
0	7000	0.386934
0	7000	0.388017
0	7000	0.385223
0	10000	0.449999
0	10000	0.47505
0	10000	0.476249
1	1000	0.089302
1	1000	0.087467
1	1000	0.094385
1	4000	0.26788
1	4000	0.26862
1	4000	0.265601
1	7000	0.401878
1	7000	0.391622
1	7000	0.383194
1	10000	0.472235
1	10000	0.470995
1	10000	0.473358

Table 11: Input for the R-code shown in Figure 40, used to test for magnetic field effect in film.

```
> x <- read.table("cuvetteDataReadout2016-03-06.csv",header=T,sep
= ",")
> MU <- x$MU
> MF <- x$MF
> netOD <- x$netOD
> ### Presage cuvette linear fit
> fit.1 <- lm(netOD ~ -1 + MU + MU:MF)
> summary(fit.1)

Call:
lm(formula = netOD ~ -1 + MU + MU:MF)

Residuals:
       Min         1Q     Median         3Q        Max 
-0.0031618 -0.0013532 -0.0003876  0.0006664  0.0023825 

Coefficients:
        Estimate Std. Error t value Pr(>|t|)    
MU     6.662e-06  7.641e-08  87.184  < 2e-16 ***
MU:MF -3.899e-07  9.864e-08  -3.952 0.000934 ***
---
Signif. codes:  0 ‘***’ 0.001 ‘**’ 0.01 ‘*’ 0.05 ‘.’ 0.1 ‘ ’ 1

Residual standard error: 0.001392 on 18 degrees of freedom
Multiple R-squared:  0.999,	Adjusted R-squared:  0.9989 
F-statistic:  8854 on 2 and 18 DF,  p-value: < 2.2e-16

> confint(fit.1, 'MU:MF', level=0.95)
              2.5 %        97.5 %
MU:MF -5.971041e-07 -1.826148e-07
```

Figure 41: R-code used for the ANOVA analysis between PRESAGE® response in B = 0 and B = 1.5 T. The p-value is shown in red.

MF	MU	OD	netOD
0	1000	-0.0044	0.0035
0	1000	-0.0029	0.005
0	4000	0.0174	0.0253
0	4000	0.0202	0.0281
0	7000	0.0371	0.045
0	7000	0.0389	0.0468
0	10000	0.0578	0.0657
0	10000	0.0611	0.069
1	1000	-0.0017	0.0062
1	1000	-0.003	0.0049
1	1000	-0.001	0.0069
1	4000	0.018	0.0259
1	4000	0.0158	0.0237
1	4000	0.016	0.0239
1	7000	0.0352	0.0431
1	7000	0.0353	0.0432
1	7000	0.036	0.0439
1	10000	0.0549	0.0628
1	10000	0.0556	0.0635
1	10000	0.0558	0.0637

Table 12: Input for the R-code shown in Figure 41, used to test for magnetic field effect in PRESAGE®.

Bibliography

1. 2010. The website of the National Cancer Institute (http://www.cancer.gov).

2. Raaymakers, B. W., J. J. Lagendijk, J. Overweg, J. G. Kok, A. J. Raaijmakers, E. M. Kerkhof, R. W. van der Put, I. Meijsing, S. P. Crijns, F. Benedosso, M. van Vulpen, C. H. de Graaff, J. Allen, and K. J. Brown. 2009. Integrating a 1.5 T MRI scanner with a 6 MV accelerator: proof of concept. *Physics in medicine and biology* 54: N229-237.

3. Raaijmakers, A. J., B. W. Raaymakers, and J. J. Lagendijk. 2005. Integrating a MRI scanner with a 6 MV radiotherapy accelerator: dose increase at tissue-air interfaces in a lateral magnetic field due to returning electrons. *Physics in medicine and biology* 50: 1363-1376.

4. Raaijmakers, A. J. E. 2008. MR-guided radiotherapy: magnetic field dose effects. Utrecht University.

5. van Heijst, T. C., M. D. den Hartogh, J. J. Lagendijk, H. J. van den Bongard, and B. van Asselen. 2013. MR-guided breast radiotherapy: feasibility and magnetic-field impact on skin dose. *Physics in medicine and biology* 58: 5917-5930.

6. Ibbott, G. S. 2010. RPC's Credentialing Programs for Clinical Trials. (AAPM Philadelphia July 2010)

7. A Molineu, P. A., S. Kry, and D. Followill. Is it feasible to tighten the criteria for IROC’s anthropomorphic phantoms? IROC-Houston QA Center.

8. Oldham, M. 2014. Methods and Techniques for Comprehensive 3D Dosimetry. In Advances in Medical Physics: 2014, D. Godfrey, S. Das, and A. Wolbars, ed. Medical Physics Pub Corp. 70-81.

9. Adamovics, J., Maryanski, M.J. . 2006. Characterisation of PRESAGE: A New 3-D Radiochromic Solid Polymer Dosemeter for Ionising Radiation. *Radiat. Prot. Dosimetry* 120: 107–112.

10. Adamson, J., Newton, J., Yang, Y., Steffey, B., Cai, J., Adamovics, J., Oldham, M., Chino, J., Craciunescu, O. 2012. Commissioning a CT-compatible LDR Tandem and Ovoid Applicator Using Monte Carlo Calculation and 3D Dosimetry. *Med. Phys.* 39: 4515–4523.

11. Juang, T., Newton, J., Niebanck, M., Benning, R., Adamovics, J., Oldham, M. 2013. Customising PRESAGE® for Diverse Applications. *J. Phys. Conf. Ser* 444:012029.

12. Adamson, J., Y. Yang, L. Rankine, J. Newton, J. Adamovics, O. Craciunescu, and M. Oldham. 2013. Towards Comprehensive Characterization of Cs-137 Seeds Using PRESAGE® Dosimetry with Optical Tomography *J. Phys. Conf. Ser* 444:012100.

13. Bache, S., T. Juang, J. Adamovics, R. Benning, B. Koontz, K. Predmore, M. Dewhirst, and M. Oldham. 2013. WE-E-108-09: An Investigation of the Feasibility of Rodentmorphic 3D Dosimeters for Verification of Precision Micro-irradiator Treatment. *Med. Phys.* 40: 490.

14. Guo, P., J. Adamovics, and M. Oldham. 2006. A Practical Three-dimensional Dosimetry System for Radiation Therapy. *Med. Phys.* 33: 3962-3972.

15. Guo, P. Y., J. A. Adamovics, and M. Oldham. 2006. Characterization of a New Radiochromic Three-dimensional Dosimeter. *Med. Phys.* 33: 1338-1345.

16. Sakhalkar, H. S., J. Adamovics, G. Ibbott, and M. Oldham. 2009. A Comprehensive Evaluation of the PRESAGE/Optical-CT 3D Dosimetry System. *Med. Phys.* 36: 71-82.

17. Wang, Z., A. Thomas, J. Newton, G. Ibbott, J. Deasy, and M. Oldham. 2010. Dose Verification of Stereotactic Radiosurgery Treatment for Trigeminal Neuralgia with Presage 3D Dosimetry System. *J. Phys. Conf. Ser* 250.

18. Oldham, M. 2006. 3D dosimetry by optical-CT scanning. *Journal of physics. Conference series* 56: 58-71.

19. Gore, J., M. Ranade, M. Maryañski, and R. Schulz. 1996. Radiation dose distributions in three dimensions from tomographic optical density scanning of polymer gels: I. Development of an optical scanner. Physics in Medicine and Biology 41: 2695-2704.

20. De Deene, Y. 2015. Dual wavelength optical CT scanning of anthropomorphic shaped 3D dosimeters. *Journal of Physics: Conference Series* 573: 012058.

21. Papadakis AE, Z. G., Maris TG, Ripoll J, Damilakis J. A New Optical-CT Apparatus for 3-D Radiotherapy Dosimetry: Is Free Space Scanning Feasible? *Med Imag, IEEE Transa on. 2010* 29: 1204-1212.

22. Olding T, H. O., Schreiner LJ. 2010. Cone beam optical computed tomography for gel dosimetry I: scanner characterization. *Physics in medicine and biology* 2010;55: 2819-2840.

23. Juang, T. 2015. Clinical and Research Applications of 3D Dosimetry. Duke University.

24. Doran, S. J., and D. N. Yatigammana. 2012. Eliminating the need for refractive index matching in optical CT scanners for radiotherapy dosimetry: I. Concept and simulations. *Physics in medicine and biology* 57: 665-683.

25. Chisholm, K., D. Miles, L. Rankine, and M. Oldham. 2015. Investigations into the feasibility of optical-CT 3D dosimetry with minimal use of refractively matched fluids. *Medical physics* 42: 2607-2614.

26. Guo, P., J. Adamovics, and M. Oldham. 2006. A practical three-dimensional dosimetry system for radiation therapy. Med. Phys. 33: 3962.

27. Oldham, M., H. Sakhalkar, P. Guo, and J. Adamovics. 2008. An investigation of the accuracy of an IMRT dose distribution using two- and three-dimensional dosimetry techniques. *Medical physics* 35: 2072-2080.

28. Thomas, A., J. Newton, J. Adamovics, and M. Oldham. 2011. Commissioning and benchmarking a 3D dosimetry system for clinical use. *Medical physics* 38: 4846-4857.

29. Manjappa, R., S. S. Makki, R. Kumar, and R. Kanhirodan. 2015. Effects of refractive index mismatch in optical CT imaging of polymer gel dosimeters. *Medical physics* 42: 750-759.

30. Manjappa, R., S. S. Makki, R. Kumar, R. M. Vasu, and R. Kanhirodan. 2016. Fully 3D refraction correction dosimetry system. *Physics in medicine and biology* 61: 1722-1737.

31. Meijsing, I., B. W. Raaymakers, A. J. Raaijmakers, J. G. Kok, L. Hogeweg, B. Liu, and J. J. Lagendijk. 2009. Dosimetry for the MRI accelerator: the impact of a magnetic field on the response of a Farmer NE2571 ionization chamber. *Physics in medicine and biology* 54: 2993-3002.

32. Mathis, M., G. Sawakuchi, D. Flint, R. Tailor, S. Beddar, G. Ibbott, and Z. Wen. 2014. 2014 CSM / R-0175 / Effects of a strong magnetic field on selected radiation dosimeters (TLD, OSLD, EBT3 film, PRESAGE) - EPOS™. Access at: http://posterng.netkey.at/esr/viewing/index.php?module=viewing_poster&pi=126172

33. Low DA, H. W., Mutic S, Purdy JA. A technique for the quantitative evaluation of dose distributions. *Medical physics* 1998; 25: 656-661 PubMed PMID: 9608475.

34. Depuydt, T., A. Van Esch, and D. P. Huyskens. 2002. A quantitative evaluation of IMRT dose distributions: refinement and clinical assessment of the gamma evaluation. *Radiotherapy and Oncology* 62: 309-319.

35. Khalid Iqbal, K. A. G., Geoffrey Ibbott, Ryan L Grant, Saeed Ahmad Buzdar. 2014. Comparison of an anthropomorphic PRESAGE® dosimeter and radiochromic film with a commercial radiation treatment planning system for breast IMRT: a feasibility study. *Journal of Applied Clinical Medical Physics* 15(1): 363-374.

36. Sorriaux, J., A. Kacperek, S. Rossomme, J. A. Lee, D. Bertrand, S. Vynckier, and E. Sterpin. 2013. Evaluation of Gafchromic® EBT3 films characteristics in therapy photon, electron and proton beams. *Physica Medica* 29: 599-606.

37. Kirby, T. H. 1992. Uncertainty analysis of absorbed dose calculations from thermoluminescence dosimeters. *Medical physics* 19: 1427.

38. Aguirre, J., P. Alvarez, D. Followill, G. Ibbott. Analysis of Uncertainties for the RPC Remote Dosimetry Using Optically Stimulated Light Dosimetry (OSLD). IROC Houston Quality Assurance Center.

39. Devic, S., J. Seuntjens, G. Hegyi, E. B. Podgorsak, C. G. Soares, A. S. Kirov, I. Ali, J. F. Williamson, and A. Elizondo. 2004. Dosimetric properties of improved GafChromic films for seven different digitizers. *Medical physics* 31: 2392-2401.

40. Sorriaux, J., A. Kacperek, S. Rossomme, J. A. Lee, D. Bertrand, S. Vynckier, and E. Sterpin. 2013. Evaluation of Gafchromic(R) EBT3 films characteristics in therapy photon, electron and proton beams. *Physica medica : PM : an international journal devoted to the applications of physics to medicine and biology : official journal of the Italian Association of Biomedical Physics* 29: 599-606.

41. Alexander, K., C. Jechel, C. Pinter, G. Salomons, A. Lasso, G. Fichtinger, and L. Schreiner. 2015. SU-E-T-231: Cross-Validation of 3D Gamma Comparison Tools. Med. Phys. 42: 3385-3385.

42. Brady, S. L., W. E. Brown, C. G. Clift, S. Yoo, and M. Oldham. 2010. Investigation into the feasibility of using PRESAGE/optical-CT dosimetry for the verification of gating treatments. *Physics in medicine and biology* 55: 2187-2201.

43. Scherman, J. 2009. Developement and evaluation of methods for comparison of dose distributions in radiotherapy using calculated, synthetic and simulated measured dose distributions. Lund University..

VITA

Gye Won (Diane) Choi was born in Seoul, South Korea on March 14, 1990, the daughter of Ho Soon Choi and Hyeon Mi Kim. After completing her work at Daewon Foreign Languange High School, Seoul, South Korea in 2009, she entered Rice University in Houston, Texas. She received the degree of Bachelor of Science with a major in Physics and a minor in Financial Computation in Modeling from Rice in May, 2013. In August of 2013 she entered The University of Texas Graduate School of Biomedical Sciences at Houston.

Permanent address:
Olympic Seonsuchon Apt. 118-702, Oryun-dong, Songpa-gu, Seoul, South Korea